UC Irvine
UC Irvine Electronic Theses and Dissertations

Title
Indoor Navigation with Cellular Signals Utilizing Synthetic Aperture for Multipath Mitigation

Permalink
https://escholarship.org/uc/item/5ph8h5qh

Author
abdallah, ali

Publication Date
2022

Peer reviewed|Thesis/dissertation

eScholarship.org Powered by the California Digital Library
University of California

UNIVERSITY OF CALIFORNIA,
IRVINE

Indoor Navigation with Cellular Signals Utilizing Synthetic Aperture for Multipath Mitigation

THESIS

submitted in partial satisfaction of the requirements
for the degree of

MASTER OF SCIENCE

in Electrical Engineering and Computer Science

by

Ali A. Abdallah

Thesis Committee:
Professor Zaher (Zak) M. Kassas, Chair
Professor Andrei Shkel
Professor Solmaz Kia

2022

© 2022 Ali A. Abdallah

DEDICATION

To my parents Ahmad and Ghazwa; my siblings: Houda, Tarek, Shadia, Mai, Safa, Fatima, and Mohamad; and to the love of my life, Fatima. You are all with me every second.

TABLE OF CONTENTS

LIST OF FIGURES

Page

LIST OF TABLES

LIST OF ALGORITHMS

ACKNOWLEDGMENTS

I would like to thank my advisor Prof. Zak Kassas for his guidance and support in my graduate studies. I am grateful for the opportunity to be part of an amazing team with amazing minds at ASPIN lab. The things I have learned from Prof. Kassas throughout my journey are uncountable.

I would like to thank my Ph.D. committee members Prof. Andrei Shkel and Prof. Solmaz Kia for taking time to serve in the committee.

I would like to thank the National Institute of Standards and Technology (NIST) for funding my research.

I would like to thank Institute of Electrical and Electronics Engineers (IEEE) and Institute of Navigation (ION) for giving me the chance to present my work to the rest of the community by publishing my conference and journal papers.

I would like to thank my friends and colleagues: Joe, Kimia, and Joshua for their support throughout my research journey and for all the helpful discussions and help with experiments.

I would like to thank my parents Ahmad and Ghazwa, my siblings: Tarek, Houda, Shadia, Mai, Safa, Fatima, and Mohamad, for their tremendous support and hope they had given to me.

Finally, my warm and heartfelt thanks goes to the love of my life, Fatima. She has stood by me through all my travails, my absences, my fits of pique and impatience. I am forever grateful to her.

ABSTRACT OF THE THESIS

Indoor Navigation with Cellular Signals Utilizing Synthetic Aperture for Multipath Mitigation

By

Ali A. Abdallah

Master of Science in Electrical Engineering and Computer Science

University of California, Irvine, 2022

Professor Zaher (Zak) M. Kassas, Chair

People nowadays spend a tremendous amount of time in indoor structures, causing them to be known as the "indoor generation." For example, Americans spend, on average, 90% of their time indoors. In light of this, demand for accurate indoor navigation and localization systems has been more than ever before. Not only accurate indoor navigation enables emerging applications, e.g., location-based services (LBS), it is vital for public safety, e.g., first responders. Numerous competing approaches have been proposed over the past couple of decades for indoor navigation and localization; however, there is no single technology that has emerged as a clear winner in solving this problem.

Among all approaches, cellular long-term evolution (LTE)-based approaches are particularly attractive as they are infrastructure-free, and if properly exploited, can lead to a practical, affordable, and accurate localization system. This is due to the inherent desirable characteristics of LTE signals [2, 3]: abundance, geometric diversity, high bandwidth (up to 20 MHz), high received power (carrier-to-noise ratio (C/N_0) ranges between 50 and 80 dB-Hz in different indoor conditions), and some of their downlink signals are free to use. Exploiting LTE-based signal for indoor localization comes with several challenges: (i) specialized receivers to opportunistically extract navigation observables from received LTE signals must

be designed, (ii) the clock biases of LTE base stations (also known as evolved Node Bs or eNodeBs) must be removed or estimated, and (iii) errors resulting from short-delay multipath must be mitigated. This Thesis addresses the aforementioned challenges. The foundational contributions of this thesis are demonstrated on showing meter-level accurate indoor navigation.

Chapter 1

Introduction

1.1 Background

People nowadays spend a tremendous amount of time in indoor structures, causing them to be known as the "indoor generation." For example, Americans spend, on average, 90% of their time indoors. In light of this, demand for accurate indoor navigation and localization systems has been more than ever before. Not only accurate indoor navigation enables emerging applications, e.g., location-based services (LBS), it is vital for public safety, e.g., first responders. This has led the U.S. Federal Communication Commission (FCC), and its equivalent international counterparts, to pass mandatory requirements for indoor location accuracy on wireless devices [4]. However, even if these requirements are met, they will not provide sufficient accuracy for first responders and LBS applications. To motivate this, consider for example the Empire State building, a 102-story Art Deco skyscraper located in midtown Manhattan, New York city (see Figure 1.1). New York city's emergency 911 system handles more than 11 million calls per year, with at least 80% of the calls originating from wireless devices [4]. Imagine an enhanced 911 (E911) call originating from a wireless device

within this building, to which emergency responders are dispatched. If met, the current FCC requirements (50-meter horizontal accuracy for 50% of all wireless calls) will only allow us to determine that the call is within this building. This is a rather large footprint for the responders to cover effectively and promptly, considering that the building is composed of 102 floors, each of which containing nearly 65 rooms. This example highlights how an accurate navigation system not only enhances public safety, but also, could save time and effort.

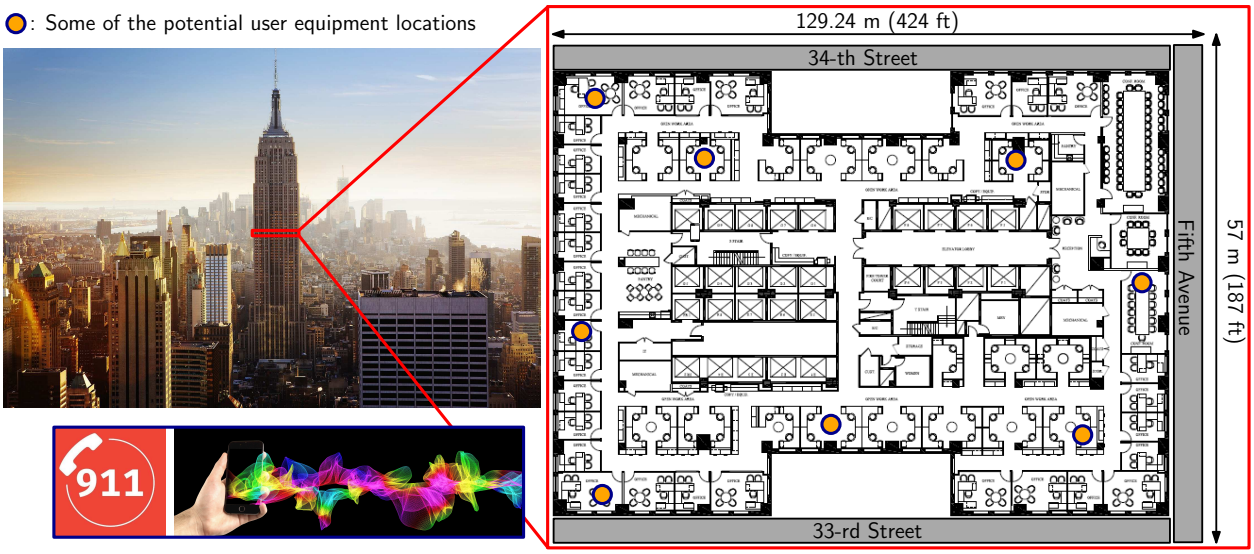

Figure 1.1: Layout of Empire State building, New York City. An emergency call from within the building, to which responders are dispatched, means that the wireless device can be in one of 102 floors, each of which contains 65 rooms (indoor layout: courtesy of Pinterest.com).

Numerous competing signal-based navigation approaches have been proposed over the past couple of decades for indoor navigation and localization; however, there is no single technology that has emerged as a clear winner in solving this problem. Some of the most noteworthy approaches to date are summarized in Table 1.1.

1.2 Related Work

Among all signal-based navigation approaches [22, 23, 24, 25], cellular long-term evolution (LTE)-based approaches are particularly attractive as they are infrastructure-free, and if properly exploited, can lead to a practical, affordable, and accurate localization system [26, 27, 28]. This is due to the inherent desirable characteristics of LTE signals [2]: abundance, geometric diversity, high bandwidth (up to 20 MHz), high received power (carrier-to-noise ratio (C/N_0) ranges between 50 and 80 dB-Hz in different indoor conditions), and some of their downlink signals are free to use. Exploiting LTE-based signal for indoor localization comes with several challenges: (i) specialized receivers to opportunistically extract navigation observables from received LTE signals must be designed, (ii) the clock biases of LTE base stations (also known as evolved Node Bs or eNodeBs) must be removed or estimated, and (iii) errors resulting from short-delay multipath must be mitigated.

Designing specialized LTE navigation receivers and approaches has been the topic of several studies over the past decade [29, 30, 31, 32, 33, 34, 35, 36, 37, 38, 39, 40, 41, 42, 43, 44, 45]. Meter-level accuracy was achieved outdoors using LTE signals on ground and aerial vehicles [18, 46, 47, 48, 49, 50, 51, 52, 53, 54, 55, 56, 57, 58], the potential of achieving of sub-meter level accuracy on aerial vehicles with LTE signals was demonstrated [59, 60, 61], and the viability of navigating exclusively in with LTE signals in GPS-jammed environments was established [62]. However, the performance of these receivers degrades indoors, mainly due to short-delay multipath effects [3, 63].

Multipath mitigation has been the subject of extensive studies in the literature, as it arises in different contexts. Some of the proposed techniques include: adaptive signal-to-noise ratio (SNR) [64], smart antennas [65], virtual multipath [66], multipath-estimating delay-locked loop (MEDLL) [67], cell-averaging constant false alarm rate (CA-CFAR) [49], sparsity-promoting regularization [68], and large-scale arrays [69].

In light of beamforming capabilities in existing and future systems (e.g., 5G), spatial discrimination offers an attractive approach to mitigate multipath by taking advantage of the geometric diversity of received signals. This can be done using physical antenna arrays [33, 70] or via synthetic aperture navigation (SAN) [20, 71, 72, 73]. Spatial discrimination techniques rely on the ability of beamforming towards the line-of-sight (LOS) direction while mitigating the multipath components. Originally termed in [74], SAN has been adopted for global navigation satellite (GNSS) signals [75]. In [76], an approach that utilizes the motion of an antenna element to enhance the detection of GNSS signals was presented, showing a 6 dB gain over a static receiver. The motion of an antenna array was exploited to minimize GNSS multipath errors in [72] and simulation results showed almost distortionless correlation peaks in the presence of one multipath signal when using a two-element antenna array.

In signal-based navigation, NLOS scenarios can stand in the way of achieving accurate navigation performance. For decades, this problem has been the subject of significant research [12, 77, 78, 79]. Tackling this problem can be divided into two consecutive parts: (a) detecting the reception scenario and (b) addressing the detected scenario algorithmically. For (a), the studies pointed out three categories of wireless channels [77]: (i) dominant LOS, (ii) weak LOS, and (iii) NLOS. For a dominant LOS, the navigation system will perform just well. For a weak LOS, several approaches were proposed in the literature to address this challenge: (1) coherent/noncoherent integration of the incoming signal [80], which requires space (motion) or frequency diversity for multipath signals to de-correlate with time; (2) constant false rate alarm (CFAR) to enhance LOS reception [49]; and (3) advanced correlation detectors [81]. The proposed system mainly addresses this scenario by utilizing the motion of the receiver to spatially suppress the NLOS components and integrate the LOS component resulting in a dominant LOS scenario for the navigation receiver. For the NLOS scenario, conventional approaches eliminate the detected NLOS outliers from the measurement vector [82, 83]. Another approach utilizes NLOS components as virtual transmitters and exploit them for navigation in a simultaneous localization and mapping (SLAM) fashion [29].

However, for detecting the reception scenario, two main approaches have been adopted in the literature: (i) LOS power discriminators and (ii) characterizing the delay profile of the signal components. The latter is more robust to signal power fluctuations; however, it requires estimating the multipath delays along with the LOS delay. For this purpose, the proposed system applies a spatial discriminator to detect NLOS outliers, in which the variation of the estimated LOS DOA is measured in vector fashion relative to previous estimates. For a pedestrian-type of motion, this approach showed a robust performance.

1.3 Challenges

There are four main challenges associated with using cellular LTE signals and SOPs in general for indoor navigation:

- The absence of published specialized receiver architectures that are capable of producing navigation observables opportunistically from LTE cellular signals.
- Multipath-induced errors. In particular, short delay multipath which introduces large errors in the code and carrier phase measurements.
- The unknown clock biases of the LTE eNodeBs which has to be estimated.
- The lack of frameworks for precise navigation with such signals.

1.4 Contributions and Dissertation Outline

The thesis is organized by contributions, which are as follows:

Chapter 2: Cellular LTE Signal Modeling and Receiver Design

This chapter describes the LTE signal structure and develops a precise low-level signal model for optimal extraction of relevant navigation and timing information from received LTE signals. Two different designs of LTE software-defined receivers (SDRs), namely a code phase-based receiver and a carrier phase-based receiver, are presented and assessed experimentally indoors with LTE signals. The developed SDR was used to evaluate the availability and strength of received LTE signals indoors in different conditions: different floor levels and in rooms with and without windows.

Chapter 3: Multipath Mitigation via Synthetic Aperture Beamforming for Indoor and Deep Urban Navigation

In this chapter, a synthetic aperture navigation (SAN) system that exploits downlink cellular long-term evolution (LTE) signals and an inertial measurement unit (IMU) is developed. The system is suitable for multipath-rich environments, such as indoors and deep urban canyons. The proposed SAN system mitigates multipath via a spatial discriminator, which utilizes the motion of a single antenna element to synthesize a geometrically separated antenna array from time-separated snapshots, alleviating the need for a physical antenna array. Signals from the synthesized antenna array are used to beamform towards the line-of-sight (LOS) LTE direction, while suppressing multipath components. Different stages of the beamforming process are discussed, and the computational complexity of the proposed system is analyzed. To deal with the unknown clock biases of the LTE eNodeBs, two navigation frameworks are developed: (1) base/rover and (2) standalone rover. The proposed SAN system is validated experimentally.

Chapter 4: Conclusions

This chapter summarizes the contributions of this thesis.

The intellectual products from this dissertation are published in the following journal and conference articles.

Journal Publications

[J1] A. Abdallah and Z. Kassas (2021) "Multipath mitigation via synthetic aperture beamforming for indoor and deep urban navigation," *IEEE Transactions on Vehicular Technology*, Vol. 70, Issue 9, Jul. 2021, pp. 8838–8853.

Conference Publications

[C1] A. Abdallah, K. Shamaei, and Z. Kassas (2018) "Indoor positioning based on LTE carrier phase measurements and an inertial measurement unit," *in Proceedings of ION GNSS Conference*, Sep. 24–28, Miami, FL, pp. 3374–3384.

[C2] A. Abdallah, K. Shamaei, and Z. Kassas (2019) "Indoor localization with LTE carrier phase measurements and synthetic aperture antenna array," *in Proceedings of ION GNSS Conference*, Sep. 16–20, Miami, FL, pp. 2670–2679.

[C3] A. Abdallah and Z. Kassas (2019) "Evaluation of feedback and feedforward coupling of synthetic aperture navigation with LTE signals," *in Proceedings of IEEE Vehicular Technology Conference*, Sep. 22–25, Honolulu, HI, pp. 1–6.

[C4] A. Abdallah, K. Shamaei, and Z. Kassas (2019) "Performance characterization of an indoor localization system with LTE code and carrier phase measurements and an IMU," *in Proceedings of International Conference on Indoor Positioning and Indoor Navigation*, Sep. 30 – Oct. 3, Pisa, Italy, pp. 1–8.

Table 1.1: Existing Indoor Navigation Systems

Technology	References	Most notable results	Challenges
WiFi	[5, 6, 7]	80 percentile accuracy of 5.6 m [5].	Requires precise and up to date knowledge of WiFi access point locations. WiFi may be unavailable in emergency situations, rendering the indoor localization system unusable.
WiFi + INS[1]	[8, 9, 10]	Position RMSE[2] of 3.47 m [10].	INS requires aiding. If WiFi becomes unavailable, the INS solution diverges.
UWB[3]	[11, 12, 13, 14, 15]	Mean east and north direction errors of 0.54 m and 0.19 m, respectively. [15].	UWB requires pre-installation and suffers in non-line-of-sight (NLOS) conditions: signals get severely attenuated and multipath induces biases in the navigation solution.
RFID[4]	[16, 17]	Position error less than 0.3479 m 80% of time [17].	Requires pre-installation and has short range.
LTE	[18, 19, 20]	Position RMSE of 5.35 m with 4 eNodeBs [18]. Position RMSE of 8 m with 50% CEP[5] with 4 eNodeBs [19]. Position RMSE of 4.32 m with 6 eNodeBs in [20].	The eNodeBs are not tightly synchronized. Multipath induces biases in the navigation solution.
LTE + INS	[21]	Position RMSE of 2.92 m.	Multipath induces biases in the navigation solution. In the absence of LTE aiding, the INS solution drifts.

[1]inertial navigation system, [2]root mean-squared error, [3]ultra-wideband, [4]radio-frequency identification, [5]circular error probability.

Chapter 2

Cellular LTE Signal Modeling and Receiver Design

This chapter is organized as follows. Section 2.1 provides an overview of the cellular LTE downlink signal. Section 2.2 develops two LTE SDT for navigation: (i) code phase-based and (ii) carrier phase-based. Section 2.3 presents several experiments to evaluate the received LTE signals in different indoor condition and assess the performance of both SDR designs.

2.1 Cellular LTE Signal Structure

The LTE signal is modulated using orthogonal frequency division multiplexing (OFDM) before transmission. In OFDM, the transmitted data symbols are mapped onto multiple carrier frequencies called subcarriers. The serial data symbols $\{S_1, \ldots, S_{N_r}\}$ are first parallelized in groups of length N_r, where N_r is the number of subcarriers carrying the data. Then, each group is extended from N_r subcarriers to N_c subcarriers by zero-padding both sides of the signal. The total number of subcarriers N_c is chosen to be greater than N_r in order

to provide a guard band in the frequency-domain [84]. An inverse fast Fourier transform (IFFT) is taken at this level. Then, the last L_{CP} elements are added at the beginning of the data, which are called the cyclic prefix (CP). The CP is used to increase the reliability of communication and protect the OFDM signals from inter-symbol interference (ISI). At an LTE receiver, these steps should be executed in reverse in order to decode the transmitted serial data symbols. There are two types of transmission for LTE: (1) frequency division duplexing (FDD) and (2) time division duplexing (TDD). Due to the superior performance of FDD in terms of latency and transmission range, most cellular providers use FDD for LTE transmission. Hence, FDD LTE signals are considered in this work.

The LTE signal bandwidth is scalable from 1.4 MHz to 20 MHz with a symbol period $T_{symb} = 1/\triangle f = 66.67\,\mu$s, which corresponds to a subcarrier spacing $\triangle f = 15$ kHz (see Table 2.1). The bandwidth could take specific values among the mentioned range depending on the values of N_r and N_c. The LTE frame is composed $T_f = 10$ ms data as shown in Figure 2.1, which is divided into 10 subframes with a duration of 1 ms, where each subframe consists of 2 slots with a duration of $T_{slot} = 0.5$ ms each. A slot can be decomposed into multiple resource grids (RGs), where each RG consists of a large number of resource blocks (RBs). Then, an RB is broken down into the smallest elements of the frame, called resource elements (REs). Thus, the subcarrier and symbol are the frequency and time indices of an RE, respectively. When a UE receives the LTE signal, it must first convert the signal into the frame structure to be able to extract the transmitted information. This is achieved by first identifying the frame start time. Then, the receiver can remove the CPs and take a fast Fourier transform (FFT) of each N_c symbols. The duration of a normal CP is 5.21 μs for the first symbol of each slot and 4.69 μs for the rest of the symbols.

Table 2.1: LTE system bandwidths and number of subcarriers

Bandwidth (MHz)	**Total number of subcarriers (N_c)**	**Number of subcarriers used (N_r)**
1.4	128	72
3	256	180
5	512	300
10	1024	600
15	1536	900
20	2048	1200

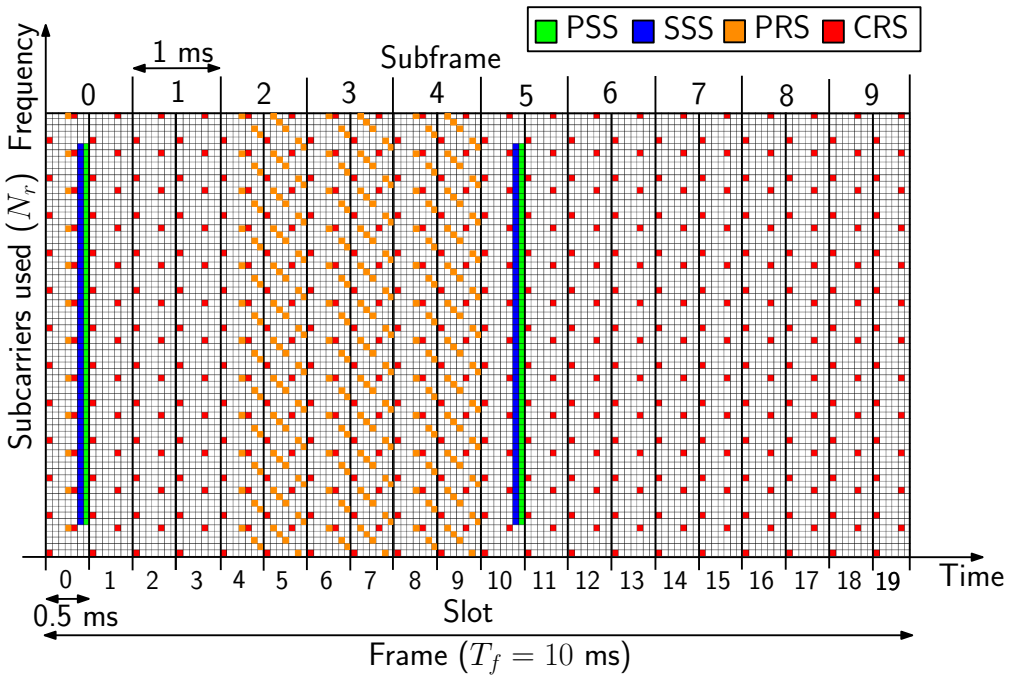

Figure 2.1: LTE frame structure

Figure 2.1 shows different reference signals that are transmitted in LTE system: (1) primary synchronization signal (PSS), (2) secondary synchronization signal (SSS), (3) cell-specific reference signal (CRS), and (4) positioning reference signal (PRS). The PSS and SSS are

transmitted to provide the frame start time and the eNodeB's cell ID to the UE. The PSS is a length-62 Zadoff-Chu sequence, which is located in the 62 middle subcarriers of the bandwidth, excluding the DC subcarriers. It is transmitted on the last symbol of slot 0 and is repeated on slot 10. The PSS sequence can take only one of the three possible sequences, each of which corresponds to an integer number $N_{ID}^{(2)} \in \{0, 1, 2\}$ representing the sector ID of the eNodeB. The SSS is an orthogonal length-62 sequence, which is transmitted in either slot 0 or 10 in the symbol preceding the PSS and on the same subcarriers as the PSS. The SSS is obtained by concatenating two maximal-length sequences scrambled by a third orthogonal sequence based on $N_{ID}^{(2)}$. There are 168 possible sequences for the SSS that are mapped to an integer number $N_{ID}^{(1)} \in \{0, \ldots, 167\}$ called the cell group identifier. Thus, the eNodeB's physical cell ID can be calculated according to [84]

$$N_{ID}^{\text{Cell}} = 3N_{ID}^{(1)} + N_{ID}^{(2)}.$$

The CRS signal is an orthogonal sequence that is scattered in time and bandwidth. It is mainly transmitted to estimate the channel frequency response (CFR). Mapping the CRS REs depends directly on the cell ID, the allocated symbol number, the slot number, and the transmission antenna port number [85]. The transmitted OFDM signal from the u-th eNodeB at the k-th subcarrier and on the i-th symbol can be expressed as

$$Y_i^{(u)}(k) = \begin{cases} S_i^{(u)}(k), & \text{if } k = m\Delta_{CRS} + \nu_{i,N_{ID}^{Cell}}, \\ D_i^{(u)}(k), & \text{otherwise}, \end{cases} \tag{2.1}$$

where $S_i^{(u)}(k)$ represents the CRS sequence; $m = 0, \cdots, M-1$; $M = \lfloor N_r/\Delta_{CRS} \rfloor$; $\Delta_{CRS} = 6$; $\nu_{i,N_{ID}^{Cell}}$ is a constant shift that depends on the cell ID and i; and $D_i^{(u)}(k)$ represents some other data signals.

In general, there is a mismatch between the estimated received symbol timing and the actual

one, which can be due to imperfect synchronization, clock drift, Doppler frequency, and/or carrier frequency offset. Assuming that the time mismatch is less than the CP duration, the received signal at the i-th symbol can be written as [86, 87]

$$R_i(k) = e^{j\pi e_f}\, e^{j2\pi(iN_t + L_{\mathrm{CP}})e_f/N_c}\, e^{j2\pi e_\theta k/N_c}\sqrt{C}\, Y_i(k)H_i(k) + W_i(k), \quad k = 0, \cdots, N_c - 1, \tag{2.2}$$

where $N_t = N_c + L_{\mathrm{CP}}$; $e_f = \frac{f_D}{\Delta f}$; f_D is the total carrier frequency offset due to the Doppler frequency, clock drift, and oscillators' mismatch; $e_\theta = \hat{\theta} - \theta$ is the symbol timing error normalized by the sampling interval $T_s = T_{symb}/N_c$; and $\hat{\theta}$ and θ are the normalized estimated and true symbol timings, respectively; $H_i(k)$ represents the channel frequency response; and $W_i(k) \sim \mathcal{CN}(0, \sigma^2)$, where $\mathcal{CN}(a, b)$ denotes the complex Gaussian distribution with mean a and variance b.

2.2 LTE Receiver Structures

In this section, the structures of two LTE receivers are presented: (1) a code phase-based receiver and (2) a carrier phase-based receiver. These receivers are an adaptation of the receiver originally introduced in [50].

2.2.1 LTE Code Phase-Based Receiver

The structure of the proposed LTE code phase-based receiver is shown in Figure 2.2. In this receiver, an OFDM-based delay-locked loop (DLL) is used to track the code phase of the CRS. The proposed receiver has three main stages, where in each stage nodes A and B are connected to nodes 1, 2, or 3.

In the first stage, where nodes A and B are connected to node 1, a coarse estimate of the

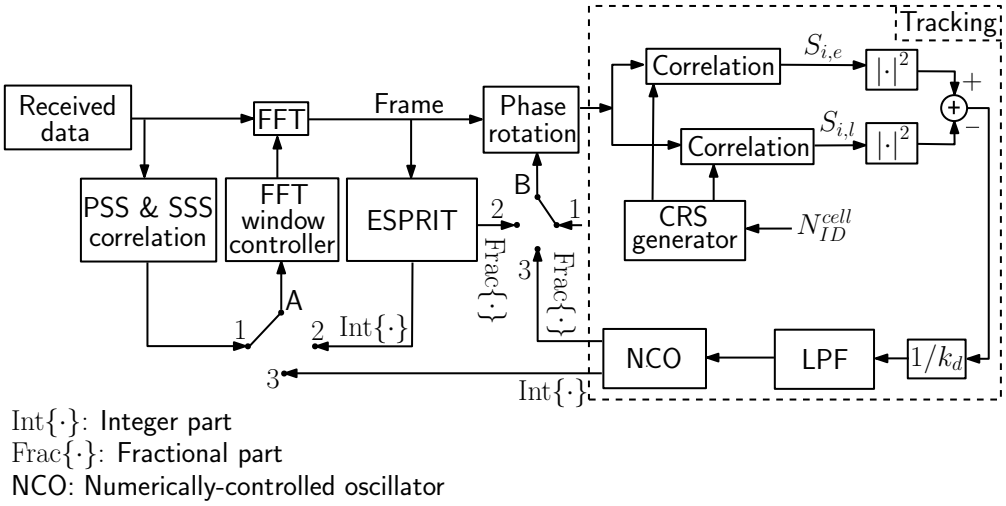

Figure 2.2: Block diagram of the proposed LTE code phase-based receiver

frame start time is obtained by acquiring the PSS and SSS. Then, the frame start time is used to control the fast Fourier transform (FFT) window timing. The CP elements are removed and an FFT is taken to convert the signal into the LTE frame structure.

In the second stage, the channel impulse response is estimated using the estimation of signal parameters by rotational invariance techniques (ESPRIT) algorithm [1]. The estimated TOA corresponding to the first path represents the line-of-sight (LOS) TOA and is used to refine the frame timing estimation. Then, the integer part of the estimated TOA is used to refine the FFT window timing and the fractional part is removed by a phase rotation in the frequency domain.

In the third stage (i.e., the tracking stage), a DLL is used to track the symbol timing. In a conventional DLL discriminator function (e.g., dot-product), correlation of the time-domain received signal with the locally generated early, late, and prompt replica of the signal is used to estimate the TOA error. However, the CRS is scattered in bandwidth, which makes it impractical to obtain its time-equivalent form. Hence, specialized DLL designed specifically for OFDM systems is used to track the CRS in LTE signals [49, 87]. In this DLL, the time-domain shift is represented as a phase rotation in the frequency-domain and the early and late correlations are obtained accordingly. Denoting the early and late correlations of

the i-th received symbol with the locally generated CRS signal by $S_{i,e}$ and $S_{i,l}$, respectively, the DLL discriminator function can be defined as

$$D_i \triangleq |S_{i,e}|^2 - |S_{i,l}|^2 \triangleq M^2 C S_d(\tilde{e}_\theta, \xi) + N_{DLL},$$

where ξ is the correlator spacing, $S_d(\tilde{e}_\theta, \xi)$ is the normalized S-curve function, and N_{DLL} is the noise component of the discriminator function as defined in [50]. For small values of timing error, the discriminator function can be approximated by a linear function of the error with slope k_d. Therefore, normalizing the output of the discriminator function by k_d and passing it through a low-pass filter (LPF) provides an estimate of the timing error, which can be integrated to provide a refined estimate of the TOA.

2.2.2 LTE Carrier Phase-Based Receiver

The structure of the proposed LTE carrier phase-based receiver is shown in Figure 2.3. In this receiver, a phase-locked loop (PLL) is implemented to track the phase of the CRS signal. Similar to the code phase-based receiver, the carrier-phase based receiver has 3 stages, where in each stage nodes A, B, and C are connected to nodes 1, 2, and 3, respectively. The first stage has common structure to the one discussed in Subsection 2.2.1. In the second stage, along with the ESPRIT algorithm, an initial estimate of the Doppler frequency is obtained by defining $z(m)$ as

$$\begin{aligned} z(m) &= R_{i+7}(k) R_i^*(k) S_{i+7}^*(k) S_i(k) \\ &= C e^{j2\pi 7 N_t e_f / N_c} |H_i(k)|^2 + W'(k), \\ \text{for} \quad & k = m\Delta_{\text{CRS}} + \nu_{i,N_{ID}^{Cell}}, \quad m = 0, \cdots, M-1. \end{aligned} \tag{2.3}$$

The above is obtained by assuming that the channel frequency response stays constant over one slot duration (i.e., 0.5 ms). Then, the initial Doppler frequency is estimated as

$$\hat{f}_D = \frac{1}{2\pi T_{slot}} \Delta\varphi, \tag{2.4}$$

$$\Delta\varphi \triangleq \arg\left[\sum_{m=0}^{M-1} z(m)\right]. \tag{2.5}$$

The initial Doppler estimate is removed from the received signal by a phase rotation on the time-domain received signal as

$$r(n) \longleftarrow e^{-j2\pi \hat{f}_D n T_s} r(n),$$

where $r(n)$ is the received signal in the time-domain.

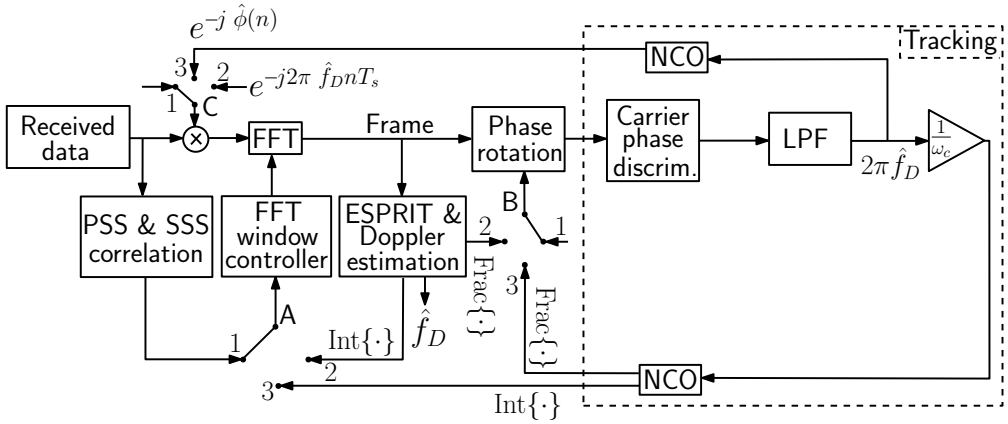

Figure 2.3: Block diagram of the proposed LTE carrier phase-based receiver

In the third stage, where nodes A, B, and C are connected to 3, the receiver tracks the phase of the received signal and produces a fine estimate of the TOA using PLL. The carrier phase discriminator function of the PLL can be defined as

$$D_{\text{PLL}} = \arg\left[\sum_{m=0}^{M-1} R'(k) S^*(k)\right],$$

$$\text{for} \quad k = m\Delta_{\text{CRS}} + \nu_{i,N_{ID}^{Cell}}, \quad m = 0, \cdots, M-1,$$

where $R'(k)$ is the frequency-domain received signal after removing the TOA and Doppler frequency estimate.

A second-order loop filter at the output of the discriminator function can be used [80, 88], which results in the rate of change of the carrier phase error $2\pi\hat{f}_D$ expressed in rad/s. By normalizing the results by angular carrier frequency ω_c, the rate of change of TOA can be obtained. Then, an integrator can be used to refine the estimate of TOA.

2.3 Experimental Evaluation

In this section, several experiments were conducted to evaluate the received LTE signals in different indoor condition and assess the performance of both SDR designs.

2.3.1 Experimental Setup and Environmental Layout

In this experiment, the base and navigator were placed outside and inside the Winston Chung Hall (WCH) building, respectively, at the University of California, Riverside. The base was equipped with 4 consumer-grade 800/1900 MHz cellular omnidirectional Laird antennas. The antennas were used to receive LTE signals at 4 different carrier frequencies: 2145 MHz, 1955 MHz, 751 MHz, and 739 MHz, which were used by three U.S. LTE cellular providers: T-Mobile, Verizon, and AT&T. Four single-channel National Instruments (NI) universal software radio peripherals (USRPs)-2920 were connected by a multiple-input multiple-output (MIMO) cable to each other to simultaneously down-mix and synchronously sample LTE signals at 10 Msps. The signals were recorded on a laptop, which was connected to the USRPs through an ethernet cable. The base could estimate its own position from GPS signals. The navigator hardware setup was similar to the base except for the USRP configuration, which was a USRP-2954R and two 2920 USRPs, which simultaneously down-mixed and

synchronously sampled LTE signals at 20 Msps. The navigator was equipped with a tactical-grade IMU (Septentrio AsteRx-i V [89]). The signals were processed in a post-processing fashion using MATLAB. Figure 2.4 shows the base and navigator experimental hardware setup.

Figure 2.5 shows the environmental layout in which the experiment was performed and the location of the eNodeBs to which the base and navigator were listening. The characteristics of the eNodeBs are shown in Table 2.2.

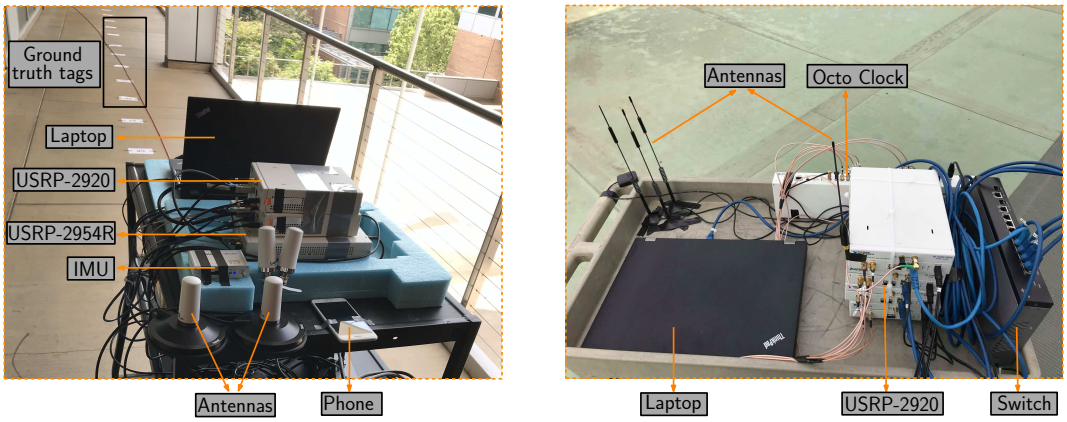

Figure 2.4: (a) Navigator and (b) Base experimental hardware setup

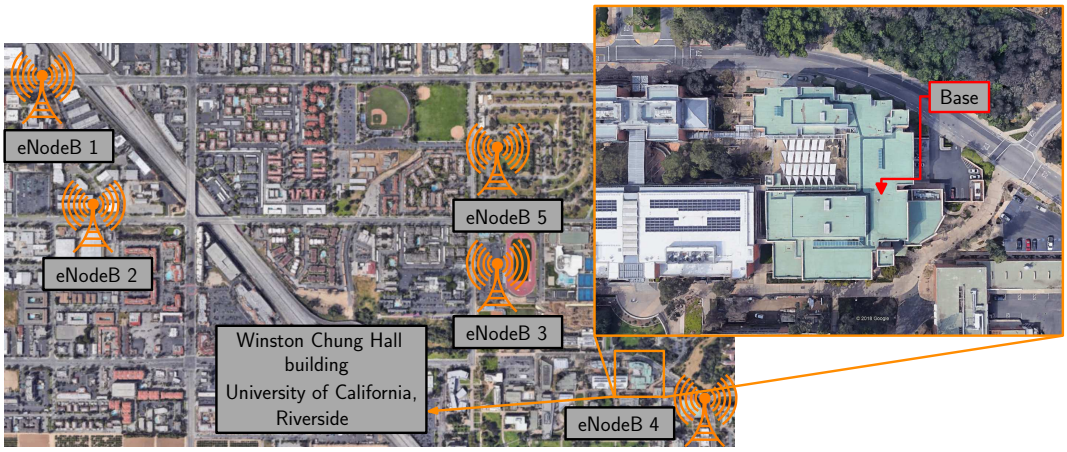

Figure 2.5: The environmental layout of the building (Winston Chung Hall at the University of California, Riverside) in which the experiment was performed and the location of the LTE eNodeBs to which the base and navigator were listening. Image: Google Earth.

Table 2.2: LTE ENodeBs' Characteristics

eNodeB	**Carrier frequency (MHz)**	N_{ID}^{Cell}	**Bandwidth (MHz)**	**Cellular provider**
1	739	144	10	AT&T
2	2145	490	20	T-Mobile
3	1955	262	20	AT&T
4	2145	383	20	T-Mobile
5	751	156	10	Verizon

2.3.2 Evaluation of Received LTE Signal's C/N_0 Indoors

Several experiments were conducted to evaluate the received LTE signals in different indoor conditions. In the first experiment, the navigator was placed in different floors, but at the same location in each floor. The navigator was also placed on the roof for comparison purposes. Figure 2.6 shows the location of the navigator in each floor. The LTE signals were recorded at each location and evaluated using the proposed receiver. Figure 2.7 shows the C/N_0 of received LTE signals in each floor and from eNodeBs 1–4 over 20 s for a stationary receiver. Table 2.3 summarizes the average C/N_0 for different eNodeBs at different floors.

Figure 2.6: Environmental layout of the floors in which the experiment was performed.

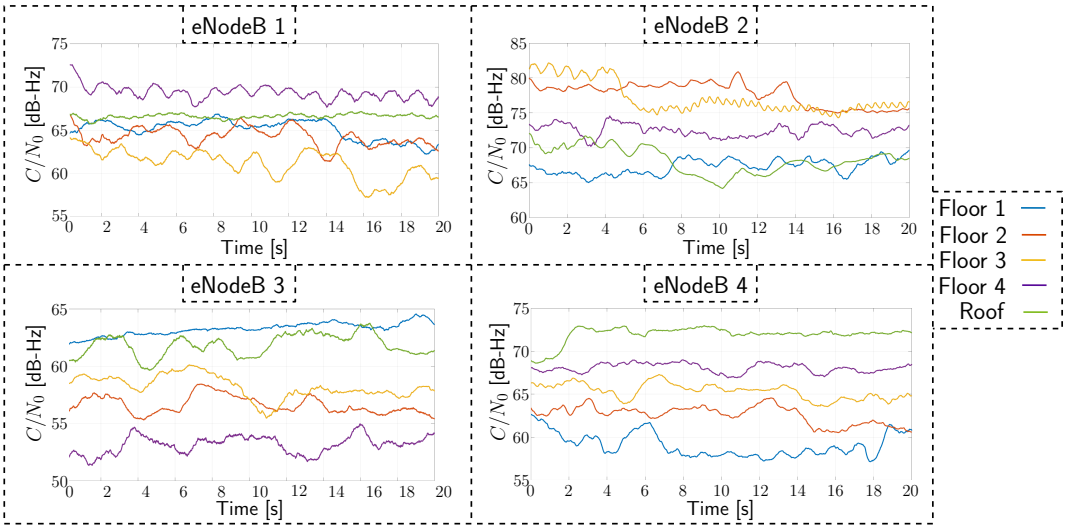

Figure 2.7: C/N_0 of received signals in floor 1–4 and the roof of the WCH building. (a)–(d) show the results for eNodeBs 1–4, respectively.

Table 2.3: Average C/N_0 for different eNodeBs at different floors

eNodeB	Floor 1	Floor 2	Floor 3	Floor 4	Roof
1	65.06	64.44	61.36	69.55	66.63
2	67.32	77.85	77.31	72.52	68.44
3	63.15	56.61	58.22	53.10	61.74
4	59.21	62.63	65.39	68.05	71.82

Next, the effect of the room structure on the received power and availability of LTE signals is evaluated. For this purpose, the LTE signals were recorded in two different rooms of the WCH building: (1) with windows access and (2) without windows access. Figure 2.8 shows the environmental layout of the rooms in which the experiment was performed.

Remarks: From the results presented in Figure 2.7, Figure 2.9, and Table 2.3, the following can be concluded:

- Table 2.3 shows that the received signal C/N_0 in different floor levels ranged between

No access to window Access to window

Figure 2.8: Environmental layout of the rooms in which the experiment was performed

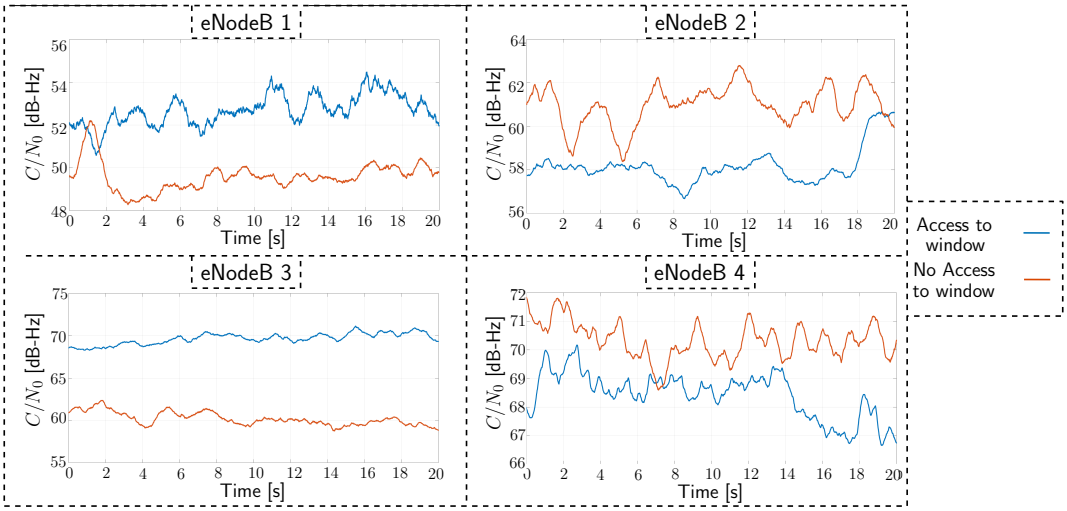

Figure 2.9: C/N_0 of received signals in rooms with window access and without window access. (a)–(d) show the results for eNodeBs 1–4, respectively.

53.10 dB-Hz and 77.85 dB-Hz, which is significantly higher than received GPS signals *outdoors*, which is typically 38–45 dB-Hz.

- It was expected to measure lower C/N_0 for lower floors. However, the results shown in Figure 2.7 suggest otherwise. this could be attributed to all obstructions that influence the propagation channel between the eNodeB and the receiver (e.g., building structure and material, constructive/destructive interference, etc.).

- It was expected to measure lower C/N_0 when the room has no access to windows. However, the results presented in Figure 2.9 suggest otherwise. Similar to the remark above, this could be attributed to the complicated propagation channel characteristics

between the eNodeB and the receiver.

2.3.3 Code Phase-Based Receiver vs. Carrier Phase-Based Receiver

The objective of this subsection is to compare the performance of the code phase-based and the carrier phase-based receivers. The navigation observables of these two receivers were fed individually to an EKF to obtain their navigation solutions. The EKF used in this subsection did not use the IMU ; instead, the EKF time-update used a velocity random walk dynamics as discussed in [49]. Figure 2.10 shows the navigation solution for both receivers. The position RMSE of the carrier phase-based receiver was 5.09 m compared to 11.76 m for the code phase-based receiver.

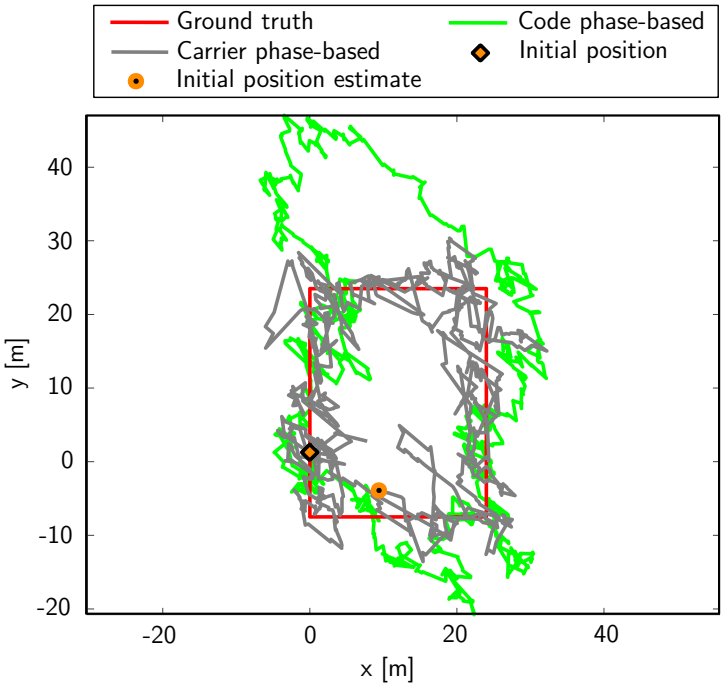

Figure 2.10: The navigator's ground truth trajectory versus the standalone code phase-based and carrier phase-based receivers

It is worth noting the following remarks pertaining to the results presented in Figure 2.10.

Remark 1: In an indoor environment, short-delay multipath highly affects the received signal. Analytical results in [50] have shown that multipath can induce meter-level error in the code phase measurement, while this error is less than a wavelength (i.e., centimeter-level) for the carrier phase measurements. This is consistent with the carrier phase-based receiver outperforming the code phase-based receiver.

Remark 2: In a carrier phase-based receiver, the integer number of cycles from the transmitter to the receiver is ambiguous and must be estimated. Several algorithms have been proposed to estimate integer ambiguities [80]. In this thesis, code phase measurements are used to initialize the integer ambiguities. Due to the low precision of code phase measurements, the accuracy of this approach is relatively lower compared to other integer ambiguity estimation algorithms.

Remark 3: Multipath can cause cycle slips in a carrier phase-based receiver, which must be detected and removed in order to achieve a reliable and accurate performance. Cycle slip detection is out of the scope of this work.

Chapter 3

Multipath Mitigation via Synthetic Aperture Beamforming for Indoor and Deep Urban Navigation

This chapter is organized as follows. Section 3.2 discusses: (i) the LTE received signal model, (ii) the LTE carrier phase-based receiver, (iii) IMU dead reckoning model, (iv) receiver clock state dynamics model, and (v) small-scale fading channel characterization. Section 3.3 presents the proposed LTE-SAN approach and discuss: (i) the LTE-SAN model, (ii) spatial smoothing, (iii) model order estimation, (iv) DOA estimation using estimation of signal parameters via rotational invariance techniques (ESPRIT), and (v) multipath mitigation via Capon's beamformer. Section 3.4 presents: (i) the base/rover framework to address eNodeBs' clock biases challenge and (ii) the LTE-SAN-IMU tightly-coupling. Section 3.5 assesses the computational complexity of the proposed system. Section 3.6 validates experimentally the proposed LTE-SAN framework in an indoor environment and presents: (i) environmental layout and experimental setup, (ii) EKF initialization and settings, (iii) navigation solution, and (iv) SAN-based beamforming results.

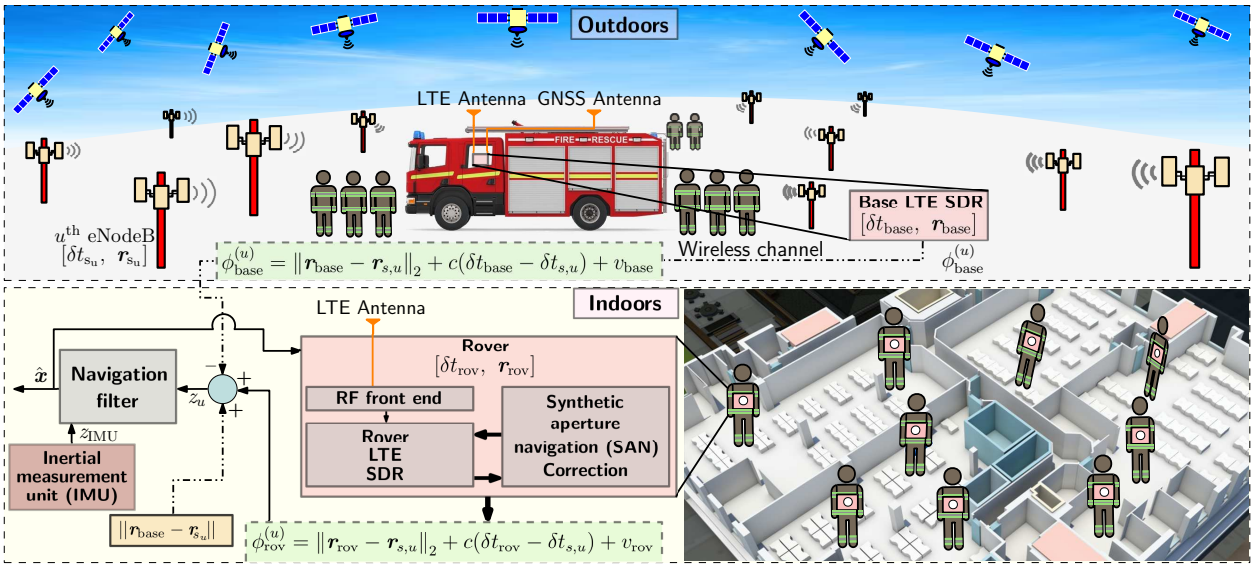

Figure 3.1: Overview of the proposed system.

3.1 Overview of Proposed System

This section presents a high-level block diagram of the proposed system is presented. The proposed system could operate in one of two navigation frameworks: (i) base/rover or (ii) standalone rover frameworks. On one hand, let's consider the base/rover framework. Imagine firefighters coming to a building, the fire truck will be outside the building. The truck is equipped with a GNSS antenna and LTE cellular antenna, which are connected to an RF front end to down-mix signals to baseband. The baseband in-phase and quadrature components of the mixer are fed to a stationary unit denoted by "base". The base is nothing but an LTE carrier phase-based receiver that collects LTE signals from multiple carrier frequencies, which correspond to multiple LTE eNodeBs in the environment. The positions of the eNodeBs are pre-surveyed and assumed to be known [90]. Moreover, the base is outdoors and has access to GNSS signals, so it can estimate its position. At the same time, the firefighters will step into the building equipped with a unit denoted by "rover." The rover includes (i) an IMU and (ii) a copy of the same LTE receiver used in the base unit; however, this LTE receiver is integrated with an SAN correction block in which the motion of the firefighters is utilized

to synthesize a geometrically-separated antenna array from time-separated snapshots. This allows for beamforming towards LOS while suppressing multipath components. The SAN correction block refines the carrier phase estimates and feed, the refined estimate either in (a) a feedforward fashion to the navigation filter or in (b) a feedback fashion to the receiver. The IMU measurements are used to propagate the states of the rover. In the base/rover framework, the "known" ranges between the base and the eNodeBs are removed and the base measurements $\{\phi_{\text{base}}^{(u)}\}_{u=1}^{U}$ are subtracted from the corresponding rover measurements $\{\phi_{\text{rov}}^{(u)}\}_{u=1}^{U}$ to eliminate the eNodeBs' clock biases, where U is the total number of eNodeBs. By eliminating the eNodeBs' clock biases, the navigation filter estimates the 2-D position, velocity, orientation, and clock bias and drift of the rover. On the other hand, in the standalone rover framework, the base unit is not there and the rover estimates the difference between its own clock bias and drift and each eNodeB clock bias and drift. Figure 3.1 presents an overview of the proposed system.

3.2 Model Description

This section presents the block diagram of the proposed system along with the various models adopted in the proposed indoor navigation system: (i) LTE signal model, (ii) LTE carrier phase-based receiver, (iii) IMU model, (iv) receiver clock state dynamics model, and (v) small-scale fading channel model.

3.2.1 LTE Signal Model

Refer to 2.1.

3.2.2 LTE Carrier Phase-Based Receiver

Refer to 2.2.2.

3.2.3 IMU Model

Relying on terrestrial LTE eNodeB exclusively for three-dimensional positioning yileds large vertical errors due to their poor geometry dilution of precision (VDOP) [91, 92]. As such, the altitude of the UE is assumed to be obtained using an external sensor (e.g., a barometer). Therefore, only the two-dimensional (2-D) position ${}^{G}\boldsymbol{r}$, velocity ${}^{G}\dot{\boldsymbol{r}}$ in the global frame G and orientation with respect to the z-axis θ_z are considered. The IMU produces the measurement vector $\boldsymbol{z}_{\text{imu}} \triangleq [\dot{\theta}_{z_{\text{imu}}}, {}^{G}\ddot{\boldsymbol{r}}_{\text{imu}}^{\mathsf{T}}]^{\mathsf{T}}$, where $\dot{\theta}_{z_{\text{imu}}}$ is the angular rate around the z-axis and ${}^{G}\ddot{\boldsymbol{r}}$ is the specific force along x- and y- axes, which are modeled according to

$$\begin{aligned}
\dot{\theta}_{z_{\text{imu}}}(n) =& \dot{\theta}_z(n) + b_{\text{gz}}(n) + n_{\text{gz}}(n), \\
\ddot{\boldsymbol{r}}_{\text{imu}}(n) =& \mathbf{R}[\theta_z(n)]\, {}^{G}\ddot{\boldsymbol{r}}(n) + \boldsymbol{b}_{\ddot{\boldsymbol{r}}}(n) + \boldsymbol{n}_{\ddot{\boldsymbol{r}}}(n),
\end{aligned}$$

where ${}^{G}\ddot{\boldsymbol{r}}$ is the 2-D acceleration of the IMU in the global frame G; $\mathbf{R}(\theta_z) \in \mathbb{R}^{2\times 2}$ is the rotation matrix representing the orientation of the body frame with respect to the global frame (as shown in Figure 3.2) and is defined as

$$\mathbf{R}(\theta_z) = \begin{bmatrix} \cos\theta_z & \sin\theta_z \\ -\sin\theta_z & \cos\theta_z \end{bmatrix};$$

$\boldsymbol{b}_{\ddot{\boldsymbol{r}}}$ represents the biases in the two accelerometers (x- and y-axes); n_{gz} and $\boldsymbol{n}_{\ddot{\boldsymbol{r}}}$ are the gyroscope's and accelerometer's measurement noise, which are modeled as zero-mean white noise sequences with covariances σ_{gz}^2 and $\sigma_{\ddot{\boldsymbol{r}}}^2\,\mathbf{I}_{2\times 2}$, respectively. The evolutions of b_{gz} and $\boldsymbol{b}_{\ddot{\boldsymbol{r}}}$

are modeled as random walk processes, i.e.,

$$b_{\text{gz}}(n+1) = b_{\text{gz}}(n) + w_{\text{gz}}(n), \tag{3.1}$$

$$\boldsymbol{b}_{\ddot{\boldsymbol{r}}}(n+1) = \boldsymbol{b}_{\ddot{\boldsymbol{r}}}(n) + \boldsymbol{w}_{\ddot{\boldsymbol{r}}}(n), \tag{3.2}$$

with $\mathbb{E}[w_{gz}] = 0$, $\mathbb{E}[\boldsymbol{w}_{\ddot{\boldsymbol{r}}}] = \mathbf{0}$, $\text{cov}[w_{gz}] = \sigma^2_{w_{gz}}$, and $\text{cov}[\boldsymbol{w}_{\ddot{\boldsymbol{r}}}] = \sigma^2_{w_{\ddot{\boldsymbol{r}}}}\mathbf{I}_{2\times 2}$.

The IMU measurements are used to evolve the position and orientation according to

$$\theta_z(n+1) = \theta_z(n) + T\dot{\theta}_z(n), \tag{3.3}$$

$${}^{G}\boldsymbol{r}(n+1) = {}^{G}\boldsymbol{r}(n) \ + T\,{}^{G}\dot{\boldsymbol{r}}(n), \tag{3.4}$$

$${}^{G}\dot{\boldsymbol{r}}(n+1) = {}^{G}\dot{\boldsymbol{r}}(n) \ + T{}^{G}\ddot{\boldsymbol{r}}(n), \tag{3.5}$$

where T is the sampling interval.

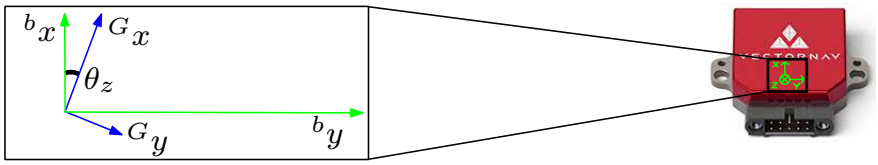

Figure 3.2: Vectornav VN-100 IMU and the relationship between the IMU body frame "b" and the Global frame "G".

3.2.4 Receiver Clock State Dynamics Model

The i-th receiver clock error state will be modeled as

$$\begin{aligned}\boldsymbol{x}_{\text{clk},i}(n+1) =& \mathbf{F}_{\text{clk}}\boldsymbol{x}_{\text{clk},i}(n) + \boldsymbol{w}_{\text{clk},i}(n), \\ &\text{for } i \in \{\text{rov}, \text{base}\},\end{aligned} \tag{3.6}$$

where $\boldsymbol{x}_{\text{clk},i} \triangleq [c\delta t_i, c\dot{\delta} t_i]^{\mathsf{T}}$ with δt and $\dot{\delta} t$ being the clock bias and clock drift, respectively, c is the speed of light, $\mathbf{F}_{\text{clk}} \triangleq \begin{bmatrix} 1 & T \\ 0 & 1 \end{bmatrix}$, and $\boldsymbol{w}_{\text{clk},i}$ is modeled as a discrete-time zero-mean white random sequence with covariance $\mathbf{Q}_{\text{clk},i}$ given by

$$\mathbf{Q}_{\text{clk},i} \triangleq \begin{bmatrix} S_{\tilde{w}_{\delta t,i}} T + S_{\tilde{w}_{\dot{\delta} t,i}} \frac{T^3}{3} & S_{\tilde{w}_{\delta t,i}} \frac{T^2}{2} \\ S_{\tilde{w}_{\dot{\delta} t,i}} \frac{T^2}{2} & S_{\tilde{w}_{\dot{\delta} t,i}} T \end{bmatrix},$$

where $S_{\tilde{w}_{\delta t,i}}$ and $S_{\tilde{w}_{\dot{\delta} t,i}}$ are the power spectra of the continuous-time process noise $\tilde{w}_{\delta t,i}$ and $\tilde{w}_{\dot{\delta} t,i}$ driving the clock bias and clock drift, respectively. The values of $S_{\tilde{w}_{\delta t,i}}$ and $S_{\tilde{w}_{\dot{\delta} t,i}}$ depend on the clock's quality [93].

3.2.5 LTE Carrier Phase Measurement Model

The carrier phase measurement, expressed in meters, made by the UE (base or rover) on the u-th LTE eNodeB can be shown to be

$$\begin{aligned} \phi_{i,u}(n) &\triangleq \lambda_u \psi i, u \\ &= \|\boldsymbol{r}_i(n) - \boldsymbol{r}_{s_u}\| + c[\delta t_i(n) - \delta t_{s_u}(n)] + b_{u,i} + n_{u,i}(n), \\ &\quad \text{for } i \in \{\text{rov}, \text{base}\}, \end{aligned}$$

where λ_u is the wavelength of the transmitted signal, $\psi_{i,u}(n)$ is the carrier phase estimate produced by the receiver, $\boldsymbol{r}_i$ is the UE's position, $\boldsymbol{r}_{s_u}$ is the u-th eNodeB's position, δt_i is the UE's clock bias, δt_{s_u} is the u-th eNodeB's clock bias, $b_{u,i}$ is the u-th eNodeB's initial carrier phase ambiguity expressed in meters, and $n_{u,i}$ is the u-th eNodeB's measurement noise modeled as a zero-mean white sequence with variance σ_u^2. The measurement noise for all eNodeBs are assumed to be independent.

The UE's position is assumed to be know at $n = 0$. Then, a new measurement is defined as

$$\begin{aligned}\phi^{'}_{i,u}(n) &= \phi_{i,u}(n) - \phi_{i,u}(0) + \|\boldsymbol{r}_i(0) - \boldsymbol{r}_{s_u}\| \\ &= \|\boldsymbol{r}_i(n) - \boldsymbol{r}_{s_u}\| + c[\delta t^{'}_i(n) - \delta t^{'}_{s_u}(n)] + n^{'}_{u,i}(n),\end{aligned}$$

where $\delta t^{'}_i(n) \triangleq (\delta t_i(n) - \delta t_i(0))$ and $\delta t^{'}_{s_u}(n) \triangleq (\delta t_{s_u}(n) - \delta t_{s_u}(0))$, and $n^{'}_{u,i}(n) \triangleq n_{u,i}(n) - n_{u,i}(0)$, where $n^{'}_{u,i}$ is modeled as $n_{u,i}$ with variance $\sigma^{'\,2}_u$. For simplicity, the "$'$" is dropped for the rest of the thesis.

3.2.6 Small-Scale Fading

The LTE received signals will be distorted due to small-scale fading if the bandwidth of transmitted signal is much greater than the coherence bandwidth B_c. The coherence bandwidth helps in defining the boundary between narrowband and wideband signals as the maximum frequency bandwidth for which the signals are still considered correlated (e.g., coherence coefficient $\geqslant 0.5$). Multipath channels are usually characterized by the power delay profile, which shows the received power versus time. The power profile could be treated as a non-normalized probability density function from which mean delay, mean-squared delay, and consequently the root mean-squared delay τ_{rms} spread can be computed. This delay and the coherence bandwidth are inversely related via the rule of thumb as [94]

$$\tfrac{1}{50\tau_{\text{rms}}} < B_c < \tfrac{1}{5\tau_{\text{rms}}}.$$

For indoor environments, experimental results showed that $10\,\text{ns} \leq \tau_{\text{rms}} \leq 50\,\text{ns}$ [95].

The Doppler spread along with coherence time provides information about the time-varying characteristic of the wireless channel. The Doppler spread B_D is a measure of the spectral broadening caused by the time rate of change of mobile radio channel and it specifies the

spectrum where the received Doppler is non-zero. For terrestrial signal-based application, the dynamics of the receiver determines B_D. If the incoming signal bandwidth is significantly greater than B_D, then the Doppler spread effect is negligible. The coherence time T_c is inversely proportional to B_D and it characterizes the frequency dispersive nature of a wireless channel in the time-domain. It represents the maximum time for which the signals are still considered to be correlated. It helps define the boundary between slow and fast fading signals. A rule of thumb to calculate T_c is

$$T_{\mathrm{C}} \approx \frac{0.423}{f_{D,\max}}. \tag{3.7}$$

where $f_{D,\max}$ is the maximum Doppler frequency introduced by the motion of the receiver, which can be calculated based on the maximum speed $v_{\max}$ of the receiver as $f_{D,\max} = v_{\max}/\lambda$, where λ is the wavelength of the transmitted signal.

3.3 Synthetic Aperture Navigation with LTE Signals

This section develops a spatial-time discriminator for navigation using LTE signals in multipath environment. The proposed approach discriminates the LOS from the multipath components using spatial information extracted from the received LTE signals. The spatial separation is performed using a synthetic aperture antenna array, where a moving single antenna element synthesizes an antenna array with time-separated elements. The proposed system assumes a synthetic aperture uniform linear array (ULA) of N time-separated antenna elements, which corresponds to N LTE snapshots (symbols) captured by the moving antenna and each separated by F symbols, where the OFDM symbol duration is $t_{\mathrm{symb}} = 66.7\,\mu$s. In practice, the UE's trajectory could be arbitrary with a time-varying speed $v(n)$, as shown in Figure 3.3. However, the proposed approach assumes $v(n) = v_c$ to be constant over a short duration of time denoted as the synthetic time $T_{\mathrm{S}} \triangleq NFt_{\mathrm{symb}}$ seconds. This assumption

is reasonable for typical pedestrian indoor motion, where the speed of a pedestrian indoors ranges from 0.5 m/s up to 2.5 m/s. The pedestrian speed v_c could be either estimated in the navigation filter or measured via an external sensor, e.g., IMU. Inhere, v_c is estimated in the navigation filter by taking the average over T_S. The skipped OFDM symbols F accounts for the physical separation between two consecutive snapshots of the moving antenna, i.e., F is determined as $F = \lfloor \frac{d}{t_{\text{symb}} v_c} \rceil$, where d is the spacing between two consecutive synthesized antenna elements and $\lfloor \cdot \rceil$ rounds the argument to the nearest integer. For design purposes, d is defined as $d \triangleq \alpha\lambda$, where α is the antenna spacing ratio to be chosen adaptively when building the synthetic antenna array.

When choosing the parameter N, few points need to be taken into consideration: (1) the stationarity of the LTE wireless channel, which differs from one environment to another and relates to the Doppler spread as discussed in Subsection 3.2.6, (2) the desired degree-of-freedom (DOF) (i.e., the number of received multipath signals that could be estimated effectively), and (3) the computational cost of the DOA estimation, which increases exponentially with N. The altitude of the receiver is assumed to be obtained using an external sensor (e.g., a barometer); i.e., only the azimuth angles $\{\phi_l^{(u)}\}_{l=0}^{L^{(u)}}$ of the impinging signals (both LOS and multipath signals) from the u-th eNodeB are estimated, where $L^{(u)}$ is the number of multipath components. Figure 3.3 depicts the proposed LTE-SAN approach with a synthetic ULA. The following subsections formulate the LTE-SAN framework, discuss DOA estimation using ESPRIT subspace-based estimator, present the NLOS detector, and analyze the beamforming process to mitigate multipath.

The proposed approach uses an ad-hoc method to choose the antenna separation, where d is chosen to satisfy the relationship $T_{\text{S}} \leq T_{\text{C}}$. Previous studies about DOA estimation have studied the optimal performance of spatial discrimination, which was achieved for spacing different from $\frac{\lambda}{2}$ [96, 97, 98]. The optimal choice was shown to depend on various factors such as: type of signal, environment, and wavelength. In [97], where short interelement separation

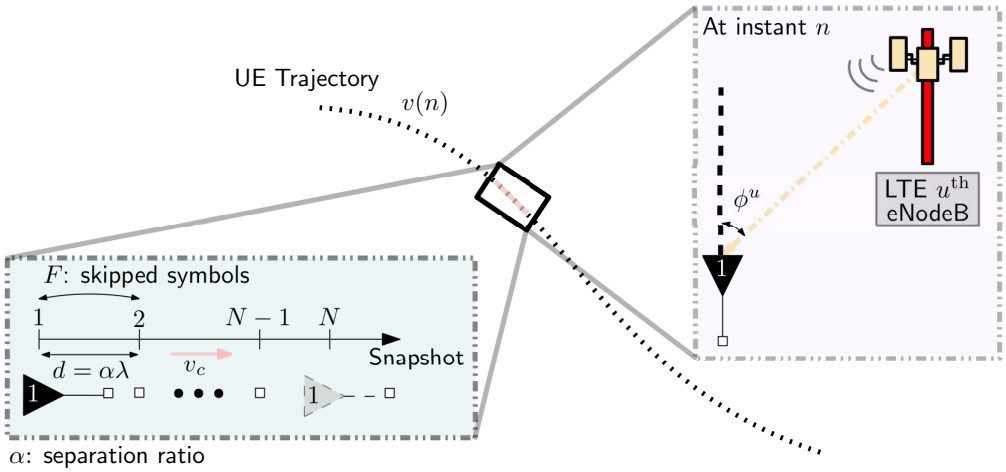

Figure 3.3: Synthetic ULA: UE trajectory, sampling process of the moving antenna, and a snapshot of the azimuth angle impinging on the antenna from the u-th eNodeB at instant n.

was utilized for CDMA signals indoors, the spatial envelope correlation was studied as a function of the antenna separation. The study showed how the spatial envelope correlation increases for $d < \frac{\lambda}{2}$, which decreases the DOA estimation accuracy. In the proposed system, spatial smoothing is applied to address this challenge by pre-filtering the incoming data to improve geometric diversity. This is achieved by dividing the synthetic antenna array into symmetric sub-antenna arrays; hence, the DOF of the system decreases, i.e., resolving fewer incoming signals. However, it is worth mentioning that choosing $d = \alpha\lambda$ has to consider the trade-off between geometric diversity, spatial correlation, and degree-of-freedom (DOF) of the spatial discriminator, while maintaining an acceptable error margin in DOA estimation.

The purpose is to design the synthetic antenna array that guarantees an acceptable DOA estimation accuracy and maximizes the size of synthetic array DOF while satisfying $T_{\text{S}} \leq T_{\text{C}}$. The proposed approach studied the DOA estimation accuracy as a function of the spacing in a Monte Carlo fashion. This study used the LTE simulator developed in [99] to simulate LTE signals assuming multipath-rich indoor environment. The study evaluated the DOA RMSE of the proposed system versus $\alpha \in [0 : 1]$ for four different LTE carrier frequencies. Figure 3.4 shows the results. It can be seen how the performance is comparable/acceptable for $\alpha \in [0.05 : 0.5]$. For $\alpha < 0.05$, as α approaches zero, the spatial diversity approaches zero

and the DOA RMSE increases exponentially. For $\alpha > 0.5$, a spatial ambiguity arises and the DOA RMSE grows logarithmically. Given these results, a lower bound α, denoted $\alpha_{\min}$, can be chosen to guarantee a specific DOA estimation accuracy. For instance, an accuracy of 10° was considered in this application, which results in $\alpha_{\min} \triangleq 0.05$ and $d_{\min} = \alpha_{\min}\lambda$. Then, the skipped LTE symbols between two consecutive snapshots and the maximum size of the synthetic array (maximum DOF) are obtained as

$$F = \left\lfloor \frac{d_{\min}}{t_{\text{symb}} v_c} \right\rfloor \tag{3.8}$$

$$N \triangleq N_{\max} = \left\lfloor \frac{T_{\text{C}}}{F t_{\text{symb}}} \right\rfloor, \tag{3.9}$$

where $\lfloor \cdot \rfloor$ denotes the greatest integer less than the argument.

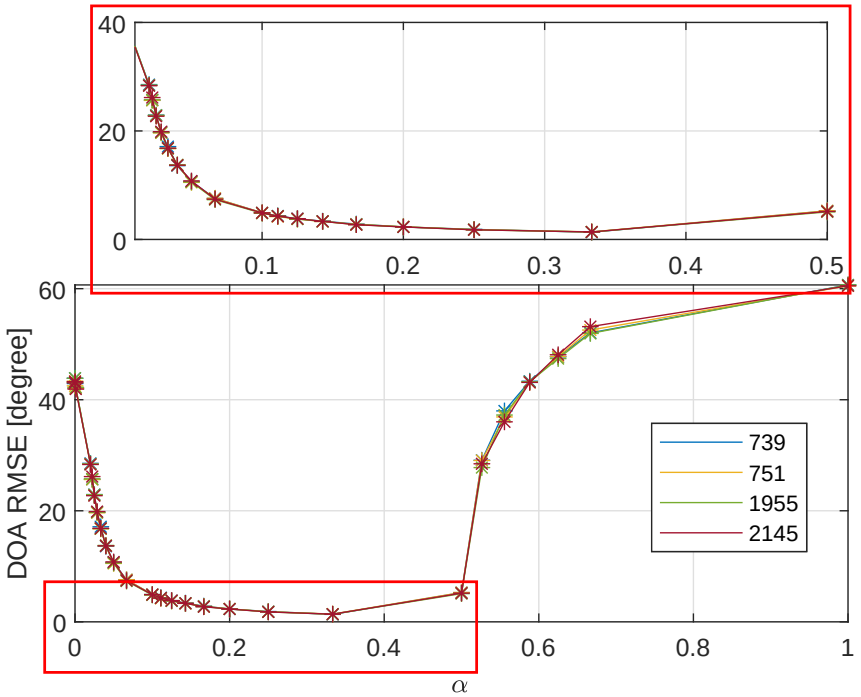

Figure 3.4: Monte Carlo study of the effect of antenna separation α on the DOA RMSE in the proposed system.

3.3.1 LTE-SAN Signal Formulation

The LTE carrier phase measurements are produced by tracking the CRS in the received LTE signals using the carrier phase-based receiver presented in Subsection 3.2.2. The CFR of the n-th received LTE frame is denoted as $H(n)$. The CFR is attractive due to high bandwidth of CRS. The proposed approach starts at the receiver's post-correlation phase. The estimated CFR of the received LTE signal from the u-th at the n-th snapshot can be expressed as

$$H(n) = \sum_{l=0}^{L^{(u)}} \alpha_l^{(u)} a_l(\phi_n^{(u)}) e^{-j2\pi f_c(\tau_l^{(u)} + n t_S/N)}, \tag{3.10}$$
$$\text{for} \quad n = 1, \cdots, N,$$

where $\alpha_l^{(u)}$ and $\tau_l^{(u)}$ are the attenuation factor and the delay, respectively, of the l-th multipath component, f_c is the carrier frequency, and $a_l(\phi_n^{(u)})$ and $a_0(\phi_n^{(u)})$ are the steering elements of the antenna element at the n-th snapshot of the l-th multipath and LOS components, respectively. The steering element of a signal represents the phase delay a plane wave experiences, evaluated at the specified antenna element. The phases are specified with respect to an arbitrary origin, where in most DOA approaches it is chosen to be the axis of the antenna array centered at the first snapshot. For instance, an n-th element having a position of $\boldsymbol{r}_n = [x_n, y_n]^{\mathsf{T}}$, the steering element for this specific element is calculated as

$$a_l(\phi_n^{(u)}) = e^{-j\langle \boldsymbol{k}, \boldsymbol{r}_n \rangle},$$

where $\boldsymbol{k}$ is the wave vector that describes the phase variation of a plane wave and $\langle \boldsymbol{a}, \boldsymbol{b} \rangle$ denotes the dot-product of vectors $\boldsymbol{a}$ and $\boldsymbol{b}$. The LOS steering element of the u-th eNodeB at the n-th snapshot, assuming knowledge of the eNodeB's position, can be obtained as

$$a_0(\phi_n^{(u)}) = e^{(n-1)j\mu^{(u)}},$$

where $\mu^{(u)} = -\frac{2\pi}{\lambda} d \sin(\phi_1^u)$ is the spatial frequency for the u-th eNodeB [70]. To simplify notation, the superscript "$^{(u)}$" will be dropped for the rest of the thesis. The complex representation of the u-th eNodeB CFR at time instance n for a single snapshot can be expressed as

$$H(n) = \boldsymbol{a}^{\mathsf{H}}(\phi_n)\boldsymbol{x}(n) + \nu(n), \tag{3.11}$$

where ν represents noise modeled as zero-mean complex white Gaussian with covariance σ^2 and

$$\begin{aligned}
\boldsymbol{a}(\phi_n) &= \left[a_0(\phi_n), \cdots, a_L(\phi_n)\right]^{\mathsf{T}}, \\
\boldsymbol{x}(n) &= \left[\alpha_0 e^{-j2\pi f_c(\tau_0 + nt_{\mathrm{S}}/N)}, \cdots, \alpha_L e^{-j2\pi f_c(\tau_L + nt_{\mathrm{S}}/N)}\right]^{\mathsf{T}}.
\end{aligned}$$

The signals captured from N snapshots, each separated by F OFDM symbols are combined as

$$\boldsymbol{H}(n) = \left[H(n), H(n+F), \cdots, H(n+(N-1)F)\right]^{\mathsf{T}}. \tag{3.12}$$

For M samples, the collected data is stacked as

$$\mathbf{H}^{(N)} = \left[\boldsymbol{H}(n), \boldsymbol{H}(n+1), \cdots, \boldsymbol{H}(n+(M-1))\right]^{\mathsf{T}}. \tag{3.13}$$

3.3.2 Preprocess Filtering, Model Order Estimation, and DOA Estimation

Different DOA estimation techniques exist in the literature, with different performance, resolution, and computational cost. Subspace-based DOA estimation techniques have better resolution than maximum-likelihood (ML) techniques. Subspace techniques basically rely

on the fact that the spatial covariance matrix (i.e., signals plus noise) of the received data spans two orthogonal subspaces, namely, the signal and noise subspaces, where the signal subspace is spanned by the larger eigenvalues of the data covariance matrix. Multiple Signal Classification (MUSIC) is one of the most popular and early proposed methods for super-resolution DOA estimation [100]. When applied to LTE DOA estimation, MUSIC has yielded high-resolution performance [20]. However, MUSIC has a high computational cost. An alternative technique with a low computational cost and high-resolution capabilities is the ESPRIT algorithm. ESPRIT requires a symmetric geometric pattern and an invariance transformation characteristic for the applied antenna design. To do so, ESPRIT divides the array into two symmetric subarrays, which can be implemented in several ways, three of which are shown in Figure 3.5. The subarrays in the red and blue boxes are defined by connection matrices denoted by $\mathbf{J}_1$ and $\mathbf{J}_2$, respectively. For linear arrays, the design shown in Figure 3.5(a) provides the highest DOF (i.e., the DOF of the new subarray) and is adopted in the proposed approach.

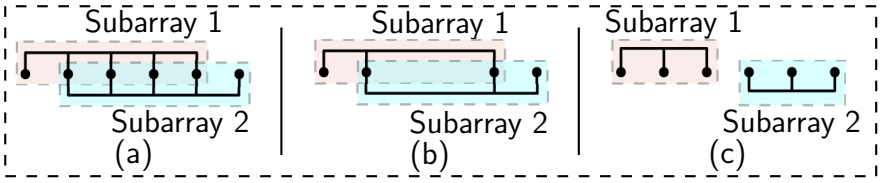

Figure 3.5: Different structures of ESPRIT subarrays: black dots represent antenna elements and red and blue boxes represent the two symmetric subarrays needed to perform the ESPRIT algorithm.

In practice, the spatial covariance matrix $\mathbf{R}_{HH}$ of the received LTE data in (3.13) is not known; however, an estimate of $\mathbf{R}_{HH}$ could be obtained as

$$\hat{\mathbf{R}}_{HH} = \frac{1}{M}\mathbf{H}^{(N)}\mathbf{H}^{(N)^{\mathsf{H}}}, \tag{3.14}$$

where $(.)^{\mathsf{H}}$ is the Hermitian operator. Algorithm 1 summarizes the steps of the standard ESPRIT algorithm. Further details about ESPRIT can be found in [1].

Algorithm 1 Standard ESPRIT Algorithm [1]

Collect data samples $\mathbf{H}^{(N)}$
Estimate the input covariance matrix $\hat{\mathbf{R}}_{HH}$ using (3.14)
Estimate the order of the system $\hat{L}+1$ (see Subsection 3.3.2)
Perform singular value decomposition $\mathbf{H}^{(N)} = \mathbf{U}\mathbf{\Sigma}\mathbf{V}^{\mathsf{H}}$ and compute $\mathbf{U}_s$, which consists of the columns of $\mathbf{U}$ corresponding to the $\hat{L}+1$ dominant singular values
Solve using the total least squares approach, the invariance equation in $\mathbf{\Psi}$

$$\mathbf{J}_1\mathbf{U}_s\mathbf{\Psi} = \mathbf{J}_2\mathbf{U}_s,$$

where $\mathbf{J}_1 = [\mathbf{I}_{(N-1)\times(N-1)}\ \mathbf{0}_{(N-1)\times 1}]$ and $\mathbf{J}_2 = [\mathbf{0}_{(N-1)\times 1}\ \mathbf{I}_{(N-1)\times(N-1)}]$
Calculate the eigenvalues of the resulting complex-valued solution

$$\mathbf{\Psi} = \mathbf{T}\mathbf{\Phi}\mathbf{T}^{-1}, \quad \text{for} \quad \mathbf{\Phi} = \text{diag}[\phi_1, \cdots, \phi_{\hat{L}+1}]$$

Extract the angular information via

$$\mu_l = \arg(\phi_l),$$
$$\phi_l = \arcsin\left(-\frac{-\lambda}{2\pi d}\mu_l\right).$$

Preprocessing Scheme: Spatial Smoothing

The DOA estimation algorithms described so far assume that the incoming signals are non-coherent. In other words, they assume that the steering matrix is full rank. If the impinging signals are highly correlated or coherent, different DOA estimation techniques will fail to provide reliable DOA estimates due to having an ill-conditioned or even singular spatial covariance matrix. In practical multipath scenarios, having highly correlated signals is very common where the incoming signals are scaled and delayed versions of each other. To overcome this challenge, the data covariance matrix is preprocessed before "feeding" it to the DOA estimation algorithm. Two well-known preprocessing schemes deal with this challenge: (1) forward-backward (FB)-averaging and (2) spatial smoothing [70]. FB-averaging is capable of resolving only the case of two coherent signals [101]. In rich multipath areas, the data may encounter more than two coherent signals. This raises the need for a more sophisticated approach to resolve this challenge. To this end, SS seems to be an attractive technique to tackle this issue. SS divides the antenna array into a smaller number of subarrays (denoted C) and the data covariance matrices obtained from each subarray are averaged. For 1-D SS, the ULA is divided into $N_{sub} = N - C + 1$ subarrays to decouple the eigenvectors of at most C coherent signals, i.e., the data is expressed as

$$\mathbf{H}_{ss}^{(N)} = \left[\mathbf{H}_{fss}^{(N)}, \mathbf{H}_{bss}^{(N)}\right],$$

where $\mathbf{H}_{fss}^{(N)}$ and $\mathbf{H}_{bss}^{(N)}$ are the forward and the backward spatially smoothed data, defined as

$$\mathbf{H}_{fss}^{(N)} = \left[\mathbf{J}_{f_1}\mathbf{H}^{(N)} \;\; \mathbf{J}_{f_2}\mathbf{H}^{(N)} \;\; \cdots \mathbf{J}_{f_C}\mathbf{H}^{(N)}\right]$$
$$\mathbf{H}_{bss}^{(N)} = \left[\mathbf{J}_{b1}\mathbf{H}^{(N)} \;\; \mathbf{J}_{b2}\mathbf{H}^{(N)} \;\; \cdots \mathbf{J}_{bC}\mathbf{H}^{(N)}\right],$$

and

$$\mathbf{J}_{f_c} = \left[\mathbf{0}_{N_{sub}\times(c-1)} \;\; \mathbf{I}_{N_{sub}} \;\; \mathbf{0}_{N_{sub}\times(N-N_{sub}-c+1)}\right]$$
$$\mathbf{J}_{bc} = \left[\mathbf{0}_{N_{sub}\times(N-N_{sub}-c+1)} \;\; \mathbf{I}_{N_{sub}} \;\; \mathbf{0}_{N_{sub}\times(c-1)}\right]$$
$$\text{for} \qquad c = 1, \cdots, C,$$

where $\mathbf{J}_{f_c}$ and $\mathbf{J}_{bc} \in \mathbb{R}^{N_{sub}\times N}$. Then, the corresponding forward and backward spatially smoothed data covariance matrices are obtained as

$$\hat{\mathbf{R}}_{HH}^{fss} = \frac{1}{CM}\mathbf{H}_{fss}^{(N)}\mathbf{H}_{fss}^{(N)\mathsf{H}}$$
$$\hat{\mathbf{R}}_{HH}^{bss} = \frac{1}{CM}\mathbf{H}_{bss}^{(N)}\mathbf{H}_{bss}^{(N)\mathsf{H}}.$$

Finally, the overall spatially smoothed data covariance matrix is obtained by averaging both the forward and backward subarrays as

$$\hat{\mathbf{R}}_{HH}^{ss} = \frac{1}{2}\left(\hat{\mathbf{R}}_{HH}^{fss} + \hat{\mathbf{R}}_{HH}^{bss}\right).$$

Note that there is a trade-off between the number of coherent signals to be resolved and the new DOF associated with the new subarray's size.

Model Order Estimators

In addition to the coherence issue of incoming signals, the number of signals $L+1$ impinging on the array was assumed to be known so far. Practically, this number is unknown and has to be estimated from the received data. The simplest way for estimating the number of signals is by estimating the number of repeated small eigenvalues other than the large ones.

In other words, if the multiplicity $\hat{q}$ of the smallest eigenvalues is found, an estimate of the number of signals, $\hat{L}+1$, can be obtained directly as

$$\hat{L} = N - \hat{q} - 1.$$

In practice, the smallest eigenvalues representing the noise power will not be identical. Instead, they will appear as a closely spaced cluster. This could be formed as a detection problem where the number of incoming signals obtained by a ULA is $L \in \{0,\, 1, \cdots,\, N-1\}$. To estimate the order of the system, one can apply the minimum description length criterion (MDL) or Akaike information theoretic criterion (AIC) [102, 103]. The estimate $\hat{L} = \text{argmin } J$, where

$$J = \begin{cases} -\ln\left[\dfrac{\prod_{i=L}^{N} \lambda_i^{\frac{1}{N-L-1}}}{\frac{1}{N-L-1}\sum_{i=L+2}^{N}\lambda_i}\right]^{(N-L-1)M} + \hat{p}_M, & \text{MDL} \\ -\ln\left[\dfrac{\prod_{i=L+2}^{N} \lambda_i^{\frac{1}{N-L-1}}}{\frac{1}{N-L-1}\sum_{i=L+2}^{KN}\lambda_i}\right]^{(N-L-1)M} + \hat{p}_A, & \text{AIC,} \end{cases}$$

where $\hat{p}_M$ and $\hat{p}_A$ are functions of number of independent parameters called penalty functions [104].

3.3.3 Multipath Mitigation: Capon's Beamformer

In order to suppress multipath signals, the only signal that is allowed to pass through the beamformer is the LOS signal. After applying beamforming to the synthetic data, the data received by array elements form a single output as follows

$$\boldsymbol{y}(n) = \boldsymbol{w}^{\mathsf{H}}\mathbf{H}^{(N)}, \tag{3.15}$$

where $\boldsymbol{w}$ is a weighting vector that is determined by optimizing some objective function subject to certain constraints. Beamforming methods differ via the choice of their objective

functions and constraints. The common strategy behind beamforming is to steer the antenna array in a particular direction at a time and evaluate the objective function, seeking an optimal complex weighting vector to weight the received signals at different snapshots. Herein, the purpose behind the proposed LTE-SAN framework is to suppress the multipath components while passing the beam where the LOS component impinges on the synthetic antenna array. To do so, different beamforming techniques could be applied. A potential beamforming technique is the Capon's method, also known as minimum variance distortionless response (MVDR) beamformer [105, 106]. The chosen weighting vector for MVDR minimizes the variance of the array output signal while passing the signal arriving from the direction of interest with no distortion which can be shown to be

$$\boldsymbol{w} = \frac{\hat{\mathbf{R}}_{HH}^{-1}\boldsymbol{a}_0(\phi)}{\boldsymbol{a}_0^{\mathsf{H}}(\phi)\hat{\mathbf{R}}_{HH}^{-1}\boldsymbol{a}_0(\phi)}, \tag{3.16}$$

where $\boldsymbol{a}_0$ is the LOS steering vector, which is obtained by taking the nearest DOA estimate $\{\phi_l\}_{l=1}^{l=\hat{L}+1}$ from Algorithm 1 to the LOS DOA estimate calculated using the current estimate of the rover's receiver and the known LTE eNodeB's position.

3.4 LTE-SAN-IMU Navigation Framework

This section presents two navigation frameworks: (i) a base/rover framework and (ii) a standalone UE framework [107, 108]. In both frameworks, LTE navigation observables are fed to the SAN-based beamformer to correct for multipath-induced errors; then, they are tightly coupled with IMU measurements using an EKF [109, 110].

3.4.1 Navigation Frameworks

One of the main challenges for navigation with LTE signals is the unknown clock biases of LTE eNodeBs by the receiver, which need to be either eliminated in a differential manner [59, 111] or estimated [112, 113, 114, 115, 116, 117, 118, 119]. This challenge can be overcome via either of the following frameworks:

Base/Rover Framework

Figure 3.1 depicts this framework in which a base is placed outdoors. The base can be mounted on a fire truck or a police car, and can estimate its own position from GNSS signals.

The base and the rover are assumed to receive signals from the same LTE eNodeBs in the environment, located at $\{\boldsymbol{r}_{s_u}\}_{u=1}^{U}$, where U is the total number of eNodeBs. The base transmits its carrier phase measurements $\phi_{\text{base}}^{(u)}$ to the rover, which subtracts it from its own $\phi_{\text{rov}}^{(u)}$ and adds the known range between the base and the u-th eNodeB $\|\boldsymbol{r}_{\text{base}} - \boldsymbol{r}_{s_u}\|$ to produce the measurement

$$z_u \triangleq \phi_{\text{rov}}^{(u)} - \phi_{\text{base}}^{(u)} + \|\boldsymbol{r}_{\text{base}} - \boldsymbol{r}_{s_u}\|.$$

Note that eNodeB clock bias is eliminated from z_u. The resulting measurements $\boldsymbol{z} \triangleq [z_1, \cdots, z_U]^{\mathsf{T}}$ are fed to the EKF.

Standalone Framework

This framework consists of a standalone rover, which estimated the difference between its own clock bias and drift and each eNodeB clock bias and drift, i.e., $[c\delta t_{\text{rov}} - c\delta t_{s_u}]_{u=1}^{U}$ and

$\left[c\dot{\delta}t_{\text{rov}} - c\dot{\delta}t_{s_u}\right]_{u=1}^{U}$, respectively. In this framework, the measurement vector that is fed to the navigation filter is $\boldsymbol{z} \triangleq \left[\phi_{\text{rov}}^{(u)}, \cdots, \phi_{\text{rov}}^{(U)}\right]^{\mathsf{T}}$.

3.4.2 LTE-SAN-IMU Coupling

The rover UE is assumed to be equipped with an IMU. An EKF is used to fuse the IMU measurements with $\boldsymbol{z}$ in a tightly-coupled fashion as shown in Figure 3.6. A barometer can be used to estimate the rover's altitude. Therefore, the EKF will only consider estimating the 2-D position of the rover.

LTE-SAN Coupling

The proposed SAN method discussed in Section 3.3 beamforms the post correlation data and suppresses the effect of multipath signals to obtain new CIRs $\{\boldsymbol{y}(k)\}_{u=1}^{U}$ with a dominant LOS peak. The new CIRs obtained are used to produce the corrected carrier phase measurements, denoted as $\boldsymbol{z}^{'}$, to replace the old observables $\boldsymbol{z}$. This is achieved by coupling the LTE receiver with the SAN approach presented in Section 3.3. The block diagram in Figure 3.6 presents two coupling schemes: (1) feedforward LTE-SAN and (2) feedback LTE-SAN.

In the feedforward LTE-SAN coupling scheme, where nodes A and B are connected to node 1, the measurements $\boldsymbol{z}$ generated by the LTE carrier phase-based receiver are processed in the proposed SAN algorithm. The corrected measurements $\boldsymbol{z}^{'}$ are fused via an EKF with IMU data.

In the feedback LTE-SAN coupling scheme, where nodes A and B are connected to node 2, the measurements $\boldsymbol{z}$ generated by the LTE carrier phase-based receiver are processed in the proposed SAN algorithm. The CIR is estimated in the tracking loop of the LTE receiver at each time instance. In the feedback scheme, the corrected CIR $\boldsymbol{y}(k)$ obtained using the

proposed approach is fed back to the tracking loops and replaces the CIR estimated using the standalone LTE receiver, which is used to produce measurements $\boldsymbol{z}^{'}$. Then, the corrected measurements $\boldsymbol{z}^{'}$ are fused via an EKF with IMU data. Note that in Figure 3.6, n and j are discrete-time instances where $k > j$.

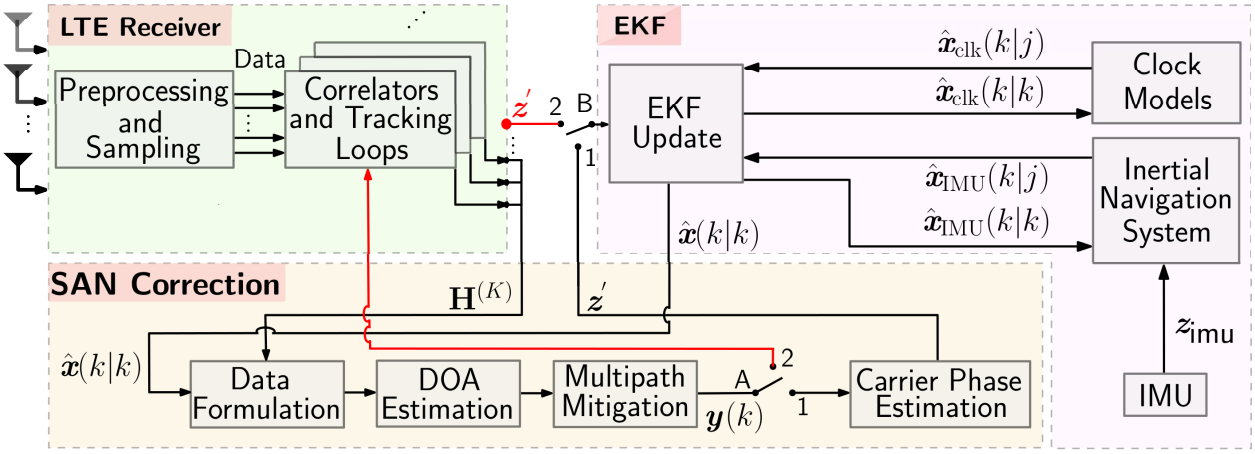

Figure 3.6: Block diagram of coupling LTE-SAN-IMU system.

EKF State

The rover's state vector $\boldsymbol{x}$ is defined as

$$\boldsymbol{x} = \left[\boldsymbol{x}_{\text{IMU}}^{\mathsf{T}}, \boldsymbol{x}_{\text{clk}}^{\mathsf{T}}\right]^{\mathsf{T}},$$

where $\boldsymbol{x}_{\text{IMU}}$ and $\boldsymbol{x}_{\text{clk}}$ are the IMU and clock state vectors, respectively.

The IMU state vector is defined as

$$\boldsymbol{x}_{\text{IMU}} \triangleq \left[\theta_z, {}^{G}\boldsymbol{r}^{\mathsf{T}}, {}^{G}\dot{\boldsymbol{r}}^{\mathsf{T}}, \boldsymbol{b}_{\boldsymbol{a}}^{\mathsf{T}}, b_{gz}\right]^{\mathsf{T}}.$$

In the base/rover framework, the clock state vector is defined as

$$\boldsymbol{x}_{\text{clk}} \triangleq \boldsymbol{x}_{\text{clk}_{\text{rov}}} - \boldsymbol{x}_{\text{clk}_{\text{base}}} = \left[c(\delta t_{\text{rov}} - \delta t_{\text{base}}), c(\dot{\delta} t_{\text{rov}} - \dot{\delta} t_{\text{base}})\right]^{\mathsf{T}},$$

where δt_{rov} and δt_{base} are the clock biases of the rover and base receivers, respectively; and $\dot{\delta} t_{\text{rov}}$ and $\dot{\delta} t_{\text{base}}$ are clock drifts of the rover and base receivers, respectively.

In the standalone rover framework, the clock state vector is defined as

$$\begin{aligned}\boldsymbol{x}_{\text{clk}} \triangleq \; & \big[c(\delta t_{\text{rov}} - \delta t_{s,1}), c(\dot{\delta} t_{\text{rov}} - \dot{\delta} t_{s,1}), \cdots, \\ & c(\delta t_{\text{rov}} - \delta t_{s,U}), c(\dot{\delta} t_{\text{rov}} - \dot{\delta} t_{s,U})\big]^{\mathsf{T}}.\end{aligned}$$

EKF Time Update

At time step n, the EKF produces an estimate of the state vector $\hat{\boldsymbol{x}}(n|j) \triangleq \mathbb{E}\left[\boldsymbol{x}(n)|\mathbf{Z}^j\right]$ along with an estimation error covariance $\mathbf{P}(n|j) \triangleq \mathbb{E}\left[\tilde{\boldsymbol{x}}(n|j)\tilde{\boldsymbol{x}}^{\mathsf{T}}(n|j)\right]$, where $n \geq j$; $\mathbf{Z}^j \triangleq \{\boldsymbol{z}(l)\}_{l=1}^{j}$; and $\tilde{\boldsymbol{x}}(n|j) \triangleq \boldsymbol{x}(n) - \hat{\boldsymbol{x}}(n|j)$ is the estimation error.

The EKF time update of the IMU states can be calculated via Euler integration as

$$\begin{aligned}\hat{\theta}_z(n+1|j) &= \hat{\theta}_z(n|j) + T\left(\hat{\dot{\theta}}_z(n|j) - \hat{b}_{\text{gz}}(n|j)\right) \\ \hat{\boldsymbol{r}}(n+1|j) &= \hat{\boldsymbol{r}}(n|j) \; + T\,\hat{\dot{\boldsymbol{r}}}(n|j) \\ \hat{\dot{\boldsymbol{r}}}(n+1|j) &= \hat{\dot{\boldsymbol{r}}}(n|j) \; + \Delta\hat{\dot{\boldsymbol{r}}} \\ \hat{b}_{gz}(n+1|j) &= \hat{b}_{gz}(n|j) \\ \hat{\boldsymbol{b}}_{\boldsymbol{a}}(n+1|j) &= \hat{\boldsymbol{b}}_{\boldsymbol{a}}(n|j),\end{aligned}$$

where T is the IMU sampling interval; $\Delta\hat{\dot{\boldsymbol{r}}} = T\,\mathbf{R}^{\mathsf{T}}\left[\hat{\theta}_z(n|j)\right]\left[\hat{\dot{\boldsymbol{r}}}(n|j) - \hat{\boldsymbol{b}}_{\boldsymbol{a}}(n|j)\right]$;

The EKF time update of the clock state estimate is given by

$$\hat{\boldsymbol{x}}_{\text{clk}}(n+1|j) = \mathbf{F}_{\text{clk}}\hat{\boldsymbol{x}}_{\text{clk}}(n|j). \tag{3.17}$$

The prediction error covariance matrix is given by

$$\mathbf{P}(n+1|j) = \mathbf{F}\mathbf{P}(n|j)\mathbf{F}^{\mathsf{T}} + \mathbf{Q}_d, \tag{3.18}$$

where $\mathbf{F} \triangleq \text{diag}\left[\mathbf{F}_{\text{IMU}}, \mathbf{F}_{\text{clk}}\right]$; $\mathbf{Q}_d = \text{diag}\left[\mathbf{Q}_{\text{IMU}}, \mathbf{Q}_{\text{clk}}\right]$; $\mathbf{F}_{\text{IMU}}$ is the linearized discrete-time IMU state transition matrix given by

$$\mathbf{F}_{\text{IMU}} = \begin{bmatrix} 1 & \mathbf{0}_{1\times 2} & \mathbf{0}_{1\times 2} & \mathbf{0}_{1\times 2} & T \\ \hat{\mathbf{I}}(n|j) & \mathbf{I}_{2\times 2} & \mathbf{0}_{2\times 2} & T\mathbf{R}\left[\theta_z(n|j)\right] & \mathbf{0}_{2\times 1} \\ \mathbf{0}_{2\times 1} & T\mathbf{I}_{2\times 2} & \mathbf{I}_{2\times 2} & \mathbf{0}_{2\times 2} & \mathbf{0}_{2\times 2} \\ \mathbf{0}_{2\times 1} & \mathbf{0}_{2\times 2} & \mathbf{0}_{2\times 2} & \mathbf{I}_{2\times 2} & \mathbf{0}_{2\times 2} \\ 0 & \mathbf{0}_{1\times 2} & \mathbf{0}_{1\times 2} & \mathbf{0}_{1\times 2} & 1 \end{bmatrix}$$

$$\hat{\mathbf{I}}(n|j) \triangleq \mathbf{J}\,\mathbf{R}[\hat{\theta_z}(n|j)]\left(\hat{\ddot{\boldsymbol{r}}}_{\text{IMU}}(n|j) + \hat{\boldsymbol{b}}_{\boldsymbol{a}}(n|j)\right),$$

with $\mathbf{J} = \begin{bmatrix} 0 & 1 \\ -1 & 0 \end{bmatrix}$; $\mathbf{Q}_{\text{IMU}}$ is the linearized discrete-time IMU state process noise covariance matrix given by

$$\mathbf{Q}_{\text{IMU}} = \frac{T}{2}\mathbf{F}_{\text{IMU}}^{\mathsf{T}}\mathbf{N}_c\mathbf{F}_{\text{IMU}} + \mathbf{N}_c,$$

where $\mathbf{N}_c \triangleq \boldsymbol{\Gamma}\mathbf{Q}_c\boldsymbol{\Gamma}^{\mathsf{T}}$; $\mathbf{Q}_c$ is the continuous-time IMU process noise covariance matrix defined as

$$\mathbf{Q}_c = \text{diag}\left[\sigma_{\text{gz}}^2, \sigma_{\boldsymbol{a}}^2\,\mathbf{I}_2, \sigma_{w_{gz}}^2, \sigma_{w_{\boldsymbol{a}}}^2\mathbf{I}_2\right];$$

and $\mathbf{\Gamma}$ is the error-state transition matrix defined as

$$\mathbf{\Gamma} = \begin{bmatrix} 1 & \mathbf{0}_{1\times 2} & \mathbf{0}_{1\times 3} \\ \mathbf{0}_{2\times 1} & \mathbf{R}[\hat{\theta}_z(n|j)] & \mathbf{0}_{2\times 3} \\ \mathbf{0}_{2\times 1} & \mathbf{0}_{2\times 2} & \mathbf{0}_{2\times 3} \\ \mathbf{0}_{3\times 1} & \mathbf{0}_{3\times 2} & \mathbf{I}_{3\times 3} \end{bmatrix}.$$

EKF Measurement Update

Once the EKF receives the measurement vector $\boldsymbol{z}^{'}$, it performs a measurement update according to

$$\hat{\boldsymbol{x}}(n+1|n+1) = \hat{\boldsymbol{x}}(n+1|j) + \mathbf{K}(n+1)\boldsymbol{\nu}(n+1), \tag{3.19}$$

where $\boldsymbol{\nu}$ and $\mathbf{K}$ are the innovation vector and Kalman gain, respectively, given by

$$\begin{aligned} \boldsymbol{\nu} &\triangleq \boldsymbol{z}^{'} - \hat{\boldsymbol{z}}^{'}, \\ \hat{z}_u &\triangleq \|\hat{\boldsymbol{r}}(n+1|j) - \boldsymbol{r}_{s_u}\| + c\Delta\hat{\delta}t(n+1|j), \\ \mathbf{K}(n+1) &\triangleq \mathbf{P}(n+1|j)\mathbf{H}^{\mathsf{T}}(n+1)\mathbf{S}^{-1}(n+1), \\ \mathbf{S}(n+1) &\triangleq \mathbf{H}(n+1)\mathbf{P}(n+1|j)\mathbf{H}(n+1)^{\mathsf{T}} + \mathbf{R}_n(n+1), \end{aligned}$$

where $u = 1, \cdots, U$ and $\mathbf{R}_n$ is the measurement noise covariance matrix. In the base/rover framework, $\mathbf{R}_n$ is given by $\mathbf{R}_n = \text{diag}\left[\sigma^2_{\text{nav}_1} + \sigma^2_{\text{base}_1}, \ldots, \sigma^2_{\text{nav}_U} + \sigma^2_{\text{base}_U}\right]$; however, in the standalone framework, it is given by $\mathbf{R}_n = \text{diag}\left[\sigma^2_{\text{nav}_1}, \ldots, \sigma^2_{\text{nav}_U}\right]$. $\mathbf{H}$ is the Jacobian matrix

defined as

$$\mathbf{H}(n+1) = \begin{bmatrix} \mathbf{H}^{(1)}(n+1) \\ \vdots \\ \mathbf{H}^{(U)}(n+1) \end{bmatrix}.$$

The estimation error covariance matrix is updated according to

$$\mathbf{P}(n+1|n+1) = [\mathbf{I} - \mathbf{K}(n+1)\mathbf{H}]\,\mathbf{P}(n+1|j).$$

Note that the LTE navigator receiver's position was assumed to be identical to the IMU's position, i.e., $\boldsymbol{r}_{\text{nav}} \equiv \boldsymbol{r}$.

3.4.3 Framework Comparison

This subsection discusses the pros and cons of each framework. The base/rover framework has less clock states to estimate, i.e., 2 states. Besides, the base and rover clocks are characterizable offline, i.e., $\mathbf{Q}_{\text{clk},i}$ are known *a priori*. However, this framework requires a base and a communication link between the rover and the base. On the other hand, the standalone framework does not need a base or a communication link. However, It as more states to estimate, i.e., $2U$ and the clocks of eNodeBs are harder to characterize *a priori*.

3.5 Computational Complexity

The computational cost of the proposed system can be divided into 3 parts: (1) the LTE receiver, (2) the SAN beamforming process, and (3) the EKF navigation filter. The complexity of the proposed software-defined radio (SDR) is on the order of $O(\text{SDR}) \approx O(N_c \log N_c)$

[120]. In the beamforming process, the main computational cost is due to the DOA estimation technique, i.e., ESPRIT algorithm. Thus, the computational cost of the feedforward SAN algorithm is $O(\text{SAN}_{\text{FF}}) \approx O(\text{ESPRIT}) = O(N(L+1)M)$ [1]. The computational cost of the EKF is $\max\{O(s^{2.376}), O(g(n+1)), O(h(n+1))\}$, where s is the number of states, $\boldsymbol{g}(n+1)$ is the dynamics model, and $\boldsymbol{h}(n+1)$ is the measurement model [121, 122]. The proposed navigation framework assumes simple propagation and measurement models, which lead to a computational complexity of $O(s^{2.376})$. It is worth mentioning that in some studies in literature, the computational complexity of EKF is assumed to be $O(s^3)$. The difference is due to different algorithms used to solve for matrix inversion or multiplication. For this study, the most efficient algorithm is considered, which gives a computational complexity of $O(s^{2.376})$. To this end, the number of states differ among the two proposed frameworks which leads to different computational cost: (i) the base/rover (B/R) framework with $O(\text{EKF}_{B/R}) = O((10)^{2.376})$ and (ii) the standalone rover (SR) framework with $O(\text{EKF}_{SR}) = O((8+2U)^{2.376})$. Therefore, the overall computational complexity of the system in the feedforward coupling scheme is approximated as

$$O_{\text{FF}} \approx \begin{cases} O(\text{SDR}) + O(\text{SAN}_{\text{FF}}) + O(\text{EKF}_{\text{B/R}}), & \text{if B/R} \\ O(\text{SDR}) + O(\text{SAN}_{\text{FF}}) + O(\text{EKF}_{\text{SR}}), & \text{if SR.} \end{cases}$$

However, for the feedback coupling scheme, the complexity can be approximated as

$$O_{\text{FB}} \approx \begin{cases} NO(\text{SDR}) + O(\text{SAN}_{\text{FF}}) + O(\text{EKF}_{\text{B/R}}), & \text{if B/R} \\ NO(\text{SDR}) + O(\text{SAN}_{\text{FF}}) + O(\text{EKF}_{\text{SR}}), & \text{if SR.} \end{cases}$$

Table 3.1: LTE ENodeBs' Characteristics

eNodeB	**Carrier frequency (MHz)**	N_{ID}^{Cell}	**Bandwidth (MHz)**	**Cellular provider**
1	739	144	10	AT&T
2	2145	490	20	T-Mobile
3	1955	262	20	AT&T
4	2145	383	20	T-Mobile
5	751	156	10	Verizon

3.6 Experimental Results

To evaluate the performance of the proposed framework, an experiment was conducted in an indoor environment: Winston Chung Hall building at the University of California, Riverside, USA. This section presents the experimental setup, analyzes the performance of the carrier phase-based receiver with and without SAN coupling, demonstrates the performance of the LTE-SAN-IMU system, and characterizes the performance of the SAN-based spatial discriminator.

3.6.1 Environmental Layout and Hardware

The base was placed on the roof of the building, while the rover was placed indoors. Both the base and rover receivers were equipped with four consumer-grade cellular omnidirectional antennas to collect LTE data at four different carrier frequencies. These frequencies corresponded to three U.S. LTE cellular providers whose characteristics are summarized in Table 3.1. The base used three single-channel National Instruments (NI) universal software radio peripherals (USRPs)-2920 to simultaneously down-mix and synchronously sample LTE signals at 10 Msps. The signals were recorded on a laptop, which was connected to the USRPs through an ethernet cable. The base location was estimated using a GPS receiver.

The rover's hardware setup was similar to the base except for the USRP configurations, which were a dual-channel USRP-2954R and two USRPs-2920. The USRPs at the rover simultaneously down-mixed and synchronously sampled LTE signals at 20 Mega-samples per second (Msps). The rover was equipped with a lower-end tactical-grade IMU (Vectornav VN-100) that outputs inertial measurements at a rate of 100 Hz. The signals were processed in a post-processing fashion. Although the SAN snapshots are taken at a higher resolution in time-domain, i.e., the duration of the OFDM symbol which is 66.7 μs. The navigation observables are obtained at the OFDM frame rate which is 100 Hz.

Several tags were placed at known locations on the ground before performing the experiment. Over the course of the experiment, a smart phone camera was used to record the location of the rover using the tags on the ground, which were later used as the ground truth. Figure 3.7 shows the base and rover experimental hardware setup.

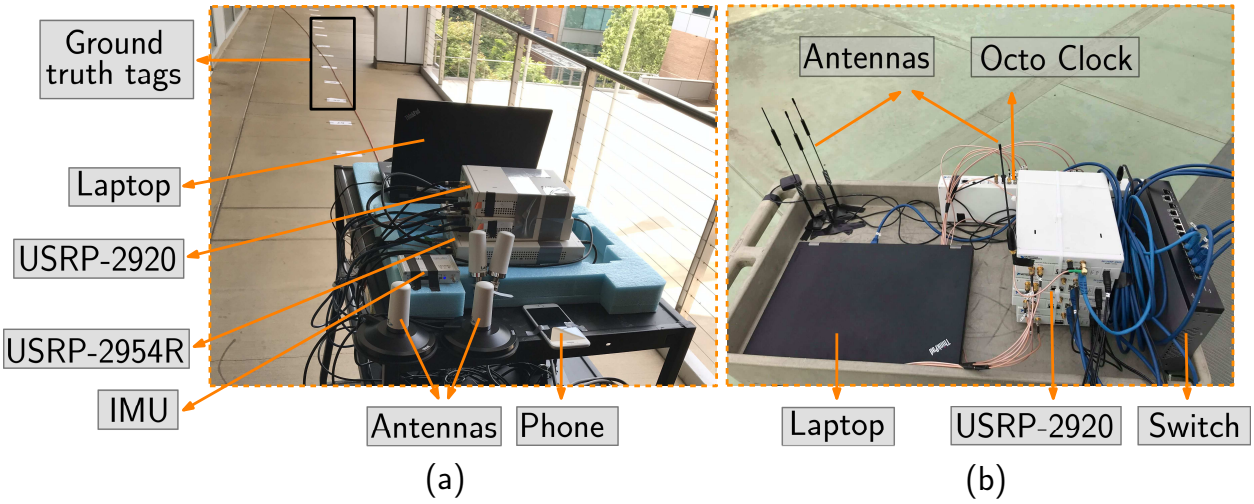

Figure 3.7: (a) Rover and (b) base experimental hardware setup.

Figure 3.8 shows the environmental layout of the experiment and the location of the eNodeBs to which the base and rover receivers were listening.

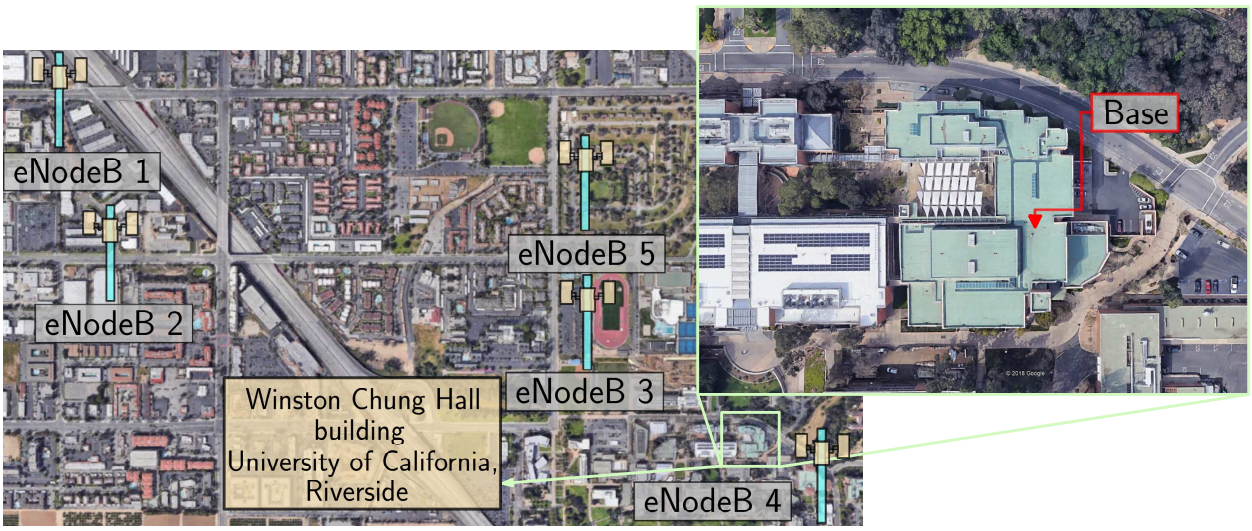

Figure 3.8: The location of the LTE eNodeBs to which the base and rover receivers were listening and the environmental layout: Winston Chung Hall building at the University of California, Riverside, USA. Image: Google Earth.

3.6.2 EKF Initialization and Settings

It was assumed that the rover entered the building from outside and that it had access to GPS signals at $k = 0$ and $k = 1$. This allows the rover to estimate its position. The receiver's clock bias $c\Delta\delta t$ and drift $c\Delta\dot{\delta}t$ were initialized using the receiver's initial position and two consecutive prior measurements. The initial clock bias and drift uncertainties were set to 1 m^2 and 0.1 $(\text{m/s})^2$, respectively. It was assumed that the receiver was equipped with a temperature-compensated crystal oscillator (TCXO) and values of $S_{\tilde{w}_{\delta t,i}}$ and $S_{\tilde{w}_{\dot{\delta} t,i}}$ were set to 4.7×10^{-20} and 7.5×10^{-20}, respectively [93]. The measurement noise variance $\{\sigma^2{}_{i,u}\}_{u=1}^{U}$ for $i \in \{\text{nav}, \text{base}\}$ were set to $\left\{c^2 \frac{\alpha_u}{(C/N_0)_u}\right\}_{u=1}^{U}$, respectively, where $(C/N_0)_u$ is the received carrier-to-noise ratio for the u-th eNodeB and $\{\alpha_u\}_{u=1}^{U}$ are tuning parameters that were chosen to be $\{5.56, 7.78, 3.33, 3.1, 3.78\} \times 10^{-12}$.

The rover's initial position and orientation were considered as the origin and orientation, respectively, of the local frame in which the rover's motion state was estimated. The gyroscope's and accelerometer's biases were initialized by taking the mean of 30 seconds of IMU data, while the rover was stationary. The rover's initial orientation, position,

and velocity were initialized using a multivariate Gaussian random generator with a mean $\mathbb{E}\left\{\left[\hat{\theta}_z(0|0), \hat{\boldsymbol{r}}^{\mathsf{T}}(0|0), \hat{\dot{\boldsymbol{r}}}^{\mathsf{T}}(0|0)\right]\right\} = [0, 0, 0, 2.2, 0.2]$ and a covariance of $\mathbf{P}(0|0) = \text{diag}[0.1, 9, 9, 1, 1]$.

3.6.3 Navigation Solution

The performance of the proposed navigation frameworks are evaluated in this subsection. Over the course of experiment, the rover traversed a trajectory of 109 m, while the base was stationary. Figure 3.9 shows the tracking results of the rover: (a) the estimated and actual carrier phases (in meters) for each eNodeB, (b) the obtained errors after removing the initial error, and (c) the measured C/N_0 of the received signal from each eNodeB over the entire experiment. The C/N_0 results are consistent with results in [3], where the C/N_0 of LTE signals from all eNodeBs was powerful over the entire indoor experiment.

Referring to Subsection 3.2.4, it is worth mentioning that the dynamics of δt_i and $\dot{\delta} t_i$ are unstable; hence, $\phi_{i,u}(n)$ is an increasing sequence as shown in Figure 3.9. Yet, the receiver is still capable of tracking the signal unless the drift of the clock is outside the dynamic range of the tracking loops, which is unlikely given the qualities of the deployed clocks. For example, Figure 3.10 shows the carrier phase error produced by the receiver of eNodeB 1 throughout the entire experiment along with the $\pm 15^\circ$ bounds, where bounded carrier phase errors were maintained. However, the clock errors should be accounted for in the navigation filter in order to produce an accurate navigation solution as discussed in Section 3.4. The same behavior is observed for other eNodeBs.

Different navigation frameworks were compared with each other's and with respect to the ground truth, namely: (1) IMU only, (2) LTE, (3) feedforward LTE-SAN, (4) feedback LTE-SAN, (5) LTE-IMU, and (6) LTE-SAN-IMU with feedback LTE-SAN. Note that the navigation solution corresponding to (2)-(6) were obtained via (i) base/rover (Figure 3.11(a)) and (ii) standalone rover framework (Figure 3.11(b)). Table 3.2 summarizes the experimental

results. It is worth noting that (i) slightly outperforms (ii), but this comes at the expense of needing a base, which may not be feasible in some applications.

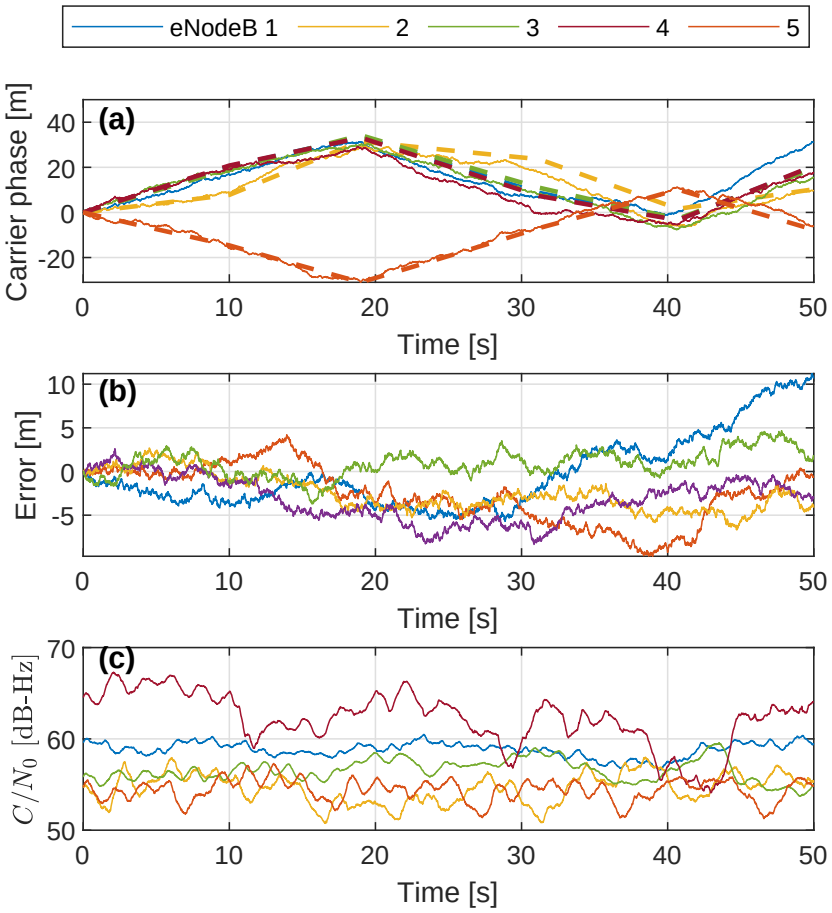

Figure 3.9: (a) Measured and actual carrier phases (in meters) for each eNodeB, plotted with solid and dashed lines,respectively. The initial values were removed for comparison purposes. (b) The obtained error between the measurement and actual carrier phases, after removing the initial error. (c) Measured C/N_0 of the received signal from each eNodeB over the entire experiment.

Figure 3.12 shows the EKF estimation error of the navigator's x-position and y-position along with the associated $\pm 2\sigma$ bounds.

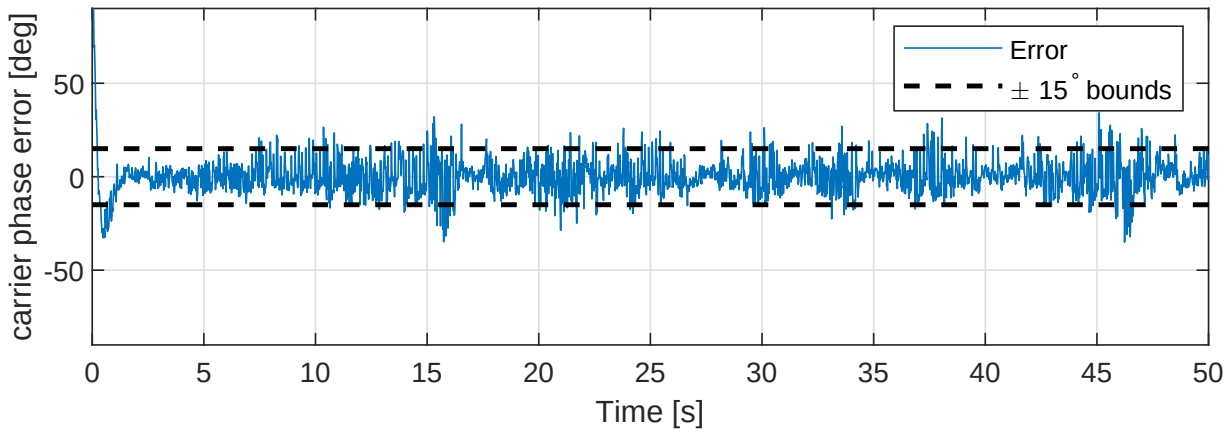

Figure 3.10: The carrier phase error for eNodeB 1 throughout the entire experiment.

3.6.4 SAN-Based Beamforming Results

This subsection analyzes the SAN-based beamforming process specifically: (i) LOS DOA RMSE of the standard ESPRIT algorithm and (ii) effect of the size of the synthetic antenna array on the localization accuracy. Figure 3.13 shows the LOS DOA RMSE of the standard ESPRIT algorithm for different LTE eNodeBs over the entire experiment. In light of these results, the accuracy of the LOS DOA estimates requires to beamform using a relatively wide beam to guarantee capturing the LOS component; however, this trade-off between capturing LOS component and suppressing multipath components may introduce more multipath-induced errors.

In the proposed framework, the size of the synthetic antenna array is a significant parameter that is related to the stationarity of the wireless channel, as discussed in Subsection 3.2.6. For the performed experiment, a study was conducted to show the effect of the size of the synthetic antenna array on the localization accuracy of the proposed system. Figure 3.14 shows the effect of N on the position RMSE of the FB-LTE-SAN for $N = \{2, 3, \cdots, 16\}$. In light of these results, three regions can be identified as follows:

- $2 \leq N \leq 7$ shaded in yellow

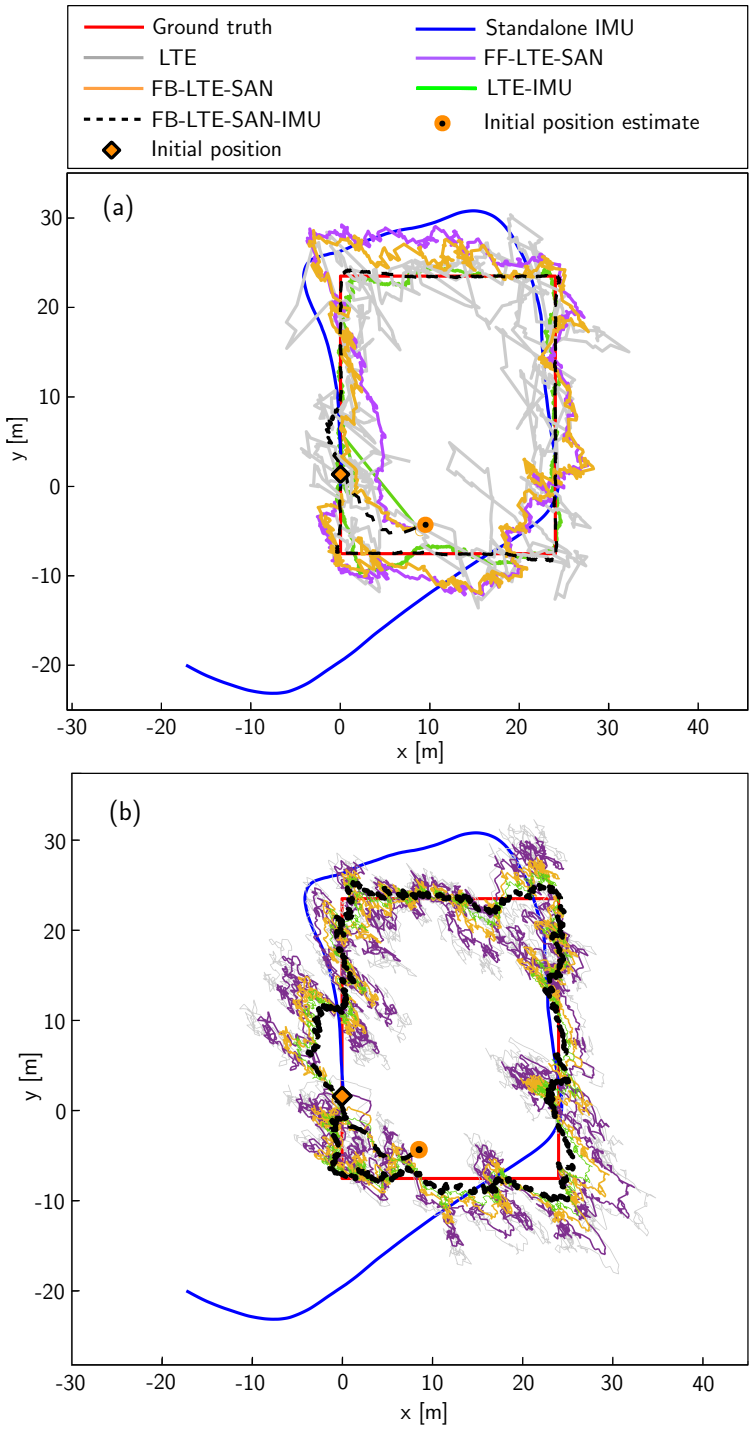

Figure 3.11: The rover's ground truth trajectory versus the navigation solution from: (1) IMU only, (2) standalone carrier phase-based LTE, (3) feedforward LTE-SAN, (4) feedback LTE-SAN, (5) LTE-IMU, and (6) LTE-SAN-IMU with feedback LTE-SAN. The base/rover framework results are shown in (a) and the standalone rover framework results are shown in (b).

Table 3.2: Indoor Navigation Performance Comparison for (i) Base/Rover and (ii) Standalone Rover.

Framework	**RMSE [m]**	**Standard deviation [m]**	**Maximum error [m]**
IMU	9.48	10.36	22.53
LTE	(i) 5.09	5.66	14.24
	(ii) 5.72	5.89	16.64
FF-LTE-SAN	(i) 4.95	2.81	12.17
	(ii) 5.58	3.29	13.77
FB-LTE-SAN	(i) 4.05	2.43	11.48
	(ii) 4.27	3.04	13.18
LTE-IMU	(i) 2.92	2.74	5.6
	(ii) 3.47	2.47	7.66
FB-LTE-SAN-IMU	(i) 1.44	1.85	3.8
	(ii) 1.80	1.30	4.2

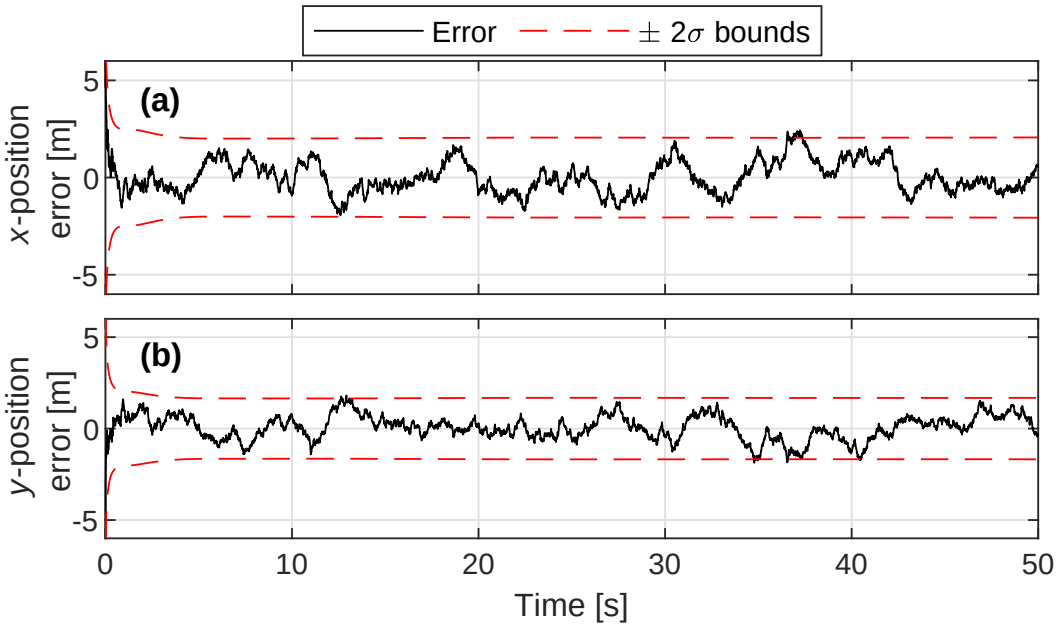

Figure 3.12: EKF estimation error of the rover's (a) x-position and (b) y-position along with the associated $\pm 2\sigma$ bounds.

- region that contains $N = 8$ shaded in green
- $N \geq 9$ shaded in red.

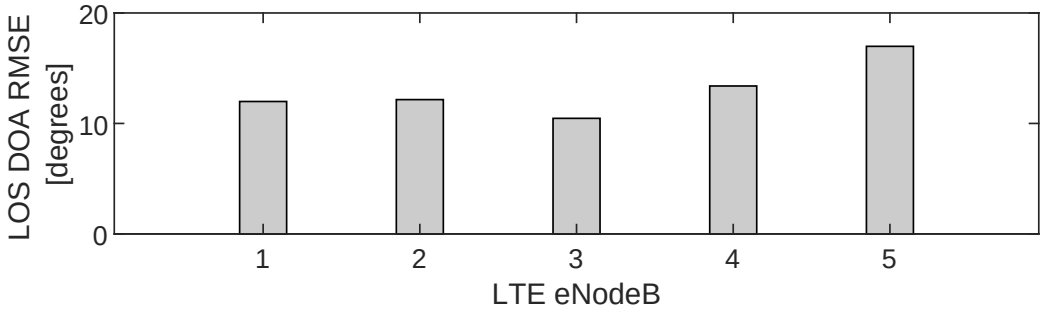

Figure 3.13: LOS DOA RMSE for each LTE eNodeB using the standard ESPRIT algorithm in the proposed SAN-based beamforming process.

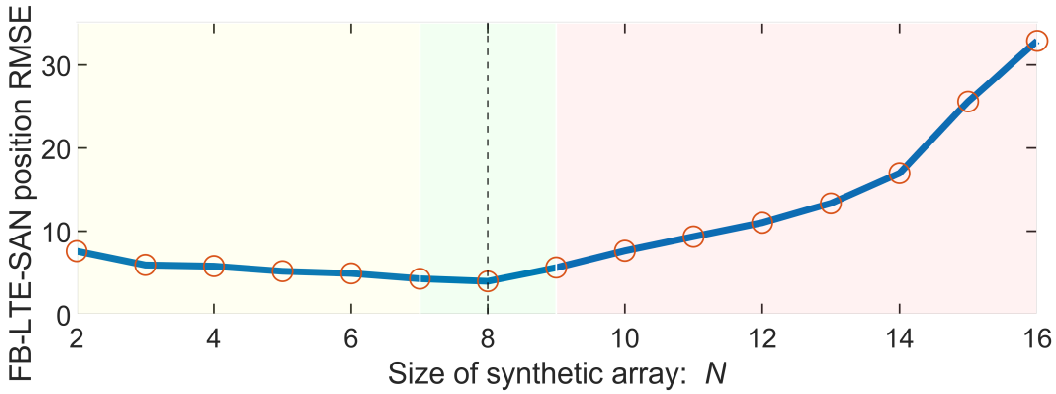

Figure 3.14: FB-LTE-SAN position RMSE versus the size of the synthetic antenna array N.

The yellow region shows a reduction in position RMSE as N increases from 2 to 7. For $N = 8$, the best performance was achieved with a position RMSE of 4.05 m. This is due to increasing the DOF of the proposed system, i.e., as N increases the proposed SAN-based beamforming process can capture more incoming signals, and consequently increase the possibility of capturing the LOS signal. In other words, the ESPRIT will estimate the DOA of the most powerful $N-1$ signals in the case where $N-1 \geq L+1$. If the LOS signal is not among the most powerful $N-1$ signals, the DOA estimates represent multipath DOA estimates and the system fails to capture the LOS components.

However, for $N \geq 9$, the red region shows a significant increase in the position RMSE. This can be justified due to the stationarity of the LTE wireless channel. In this case, the assumption of having time-separated snapshots as geometrically-spaced antenna elements does not hold anymore due to channel variations. This introduces significant error in the

SAN-based beamforming process by producing faulty DOA estimates, and consequently corrupting the beamformed data.

To justify this result, a theoretical approximation can be found from equations (3.7)-(3.9). For this purpose, (3.7) and (3.8) can be expanded as

$$T_C = \frac{0.432c}{v_{\max} f_c}, \tag{3.20}$$

$$F = \left\lfloor \frac{\alpha_{\min} c}{t_{\text{symb}} v_c f_c} \right\rfloor, \tag{3.21}$$

where f_c is the carrier frequency of the received LTE signal. Then, (3.9) can be written as

$$N_{\max} = \left\lfloor \frac{\frac{0.432c}{v_{\max} f_c}}{\left\lfloor \frac{\alpha_{\min} c}{t_{\text{symb}} v_c f_c} \right\rfloor t_{\text{symb}}} \right\rfloor, \tag{3.22}$$

$$\approx \left\lfloor \frac{0.432}{\alpha_{\min}} \cdot \frac{v_c}{v_{\max}} \right\rfloor, \tag{3.23}$$

$$= \left\lfloor 8.64 \cdot \frac{v_c}{v_{\max}} \right\rfloor, \tag{3.24}$$

where the approximation from (3.22) to (3.23) is due to fact that $\frac{\alpha_{\min} c}{t_{\text{symb}} v_c f_c} \gg 1$ for $\alpha_{\min} = 0.05$ and $f_c \in [600\ 3000]$ MHz (i.e., range of LTE frequencies). In this experiment, v_c on average was constant throughout the experiment; thus, $\frac{v_c}{v_{\max}} \approx 1$, which results in $N_{\max} \approx 8$.

Chapter 4

Conclusions

This thesis evaluated the Performance of cellular long-term evolution (LTE) signals for indoor localization. The availability and strength of received LTE signals indoors was evaluated in different conditions: different floor levels and in rooms with and without windows. It was demonstrated that the received carrier-to-noise ratio C/N_0 in all such conditions was 48-80 dB-Hz. Two different designs of LTE software-defined receivers (SDRs), namely a code phase-based receiver and a carrier phase-based receiver, were presented and assessed experimentally indoors with LTE signals. It was demonstrated that the standalone carrier phase-based receiver yielded a more precise navigation solution than the code phase-based receiver, specifically a two-dimensional (2-D) position root mean-squared error (RMSE) of 5.09 m versus 11.76 m for an indoor trajectory of 109 m traversed in 50 seconds.

Next, this thesis presented an infrastructure-free, practical, affordable, and accurate indoor navigation and localization system using downlink LTE signals and an IMU. The proposed system exploits the motion of a single antenna element to spatially discriminate LOS from multipath signals in an SAN framework, and subsequently, beamforms the incoming signals towards the LOS direction while minimizing the multipath components. The paper discussed

the carrier phase-based LTE receiver to extract the navigation observables and presented two navigation frameworks to unknown clock biases of LTE eNodeBs: (i) base/rover and (ii) standalone rover. The different stages of the SAN-based beamforming process was discussed: (i) data formulation, (ii) preprocess filtering, (iii) model order estimation, (iv) DOA estimation, and (v) multipath mitigation. An EKF-based tightly-coupled LTE-SAN-aided IMU system was developed and the computational complexity of the proposed system was studied. Experimental results were presented, in which a pedestrian-mounted receiver navigated indoors for 109 m in 50 seconds, while receiving LTE signals from 5 LTE eNodeBs. Six navigation approaches were compared: (i) IMU only, (ii) LTE only, (iii) feedforward LTE-SAN, (iv) feedback LTE-SAN, (v) LTE-IMU, and (vi) feedback LTE-SAN-IMU. The position RMSE resulting from these approaches were 9.48 m, 5.09 m, 4.95 m, 4.05 m, 2.92 m, and 1.44 m, respectively.

Bibliography

[1] R. Roy and T. Kailath, "ESPRIT-estimation of signal parameters via rotational invariance techniques," *IEEE Transactions on Acoustics, Speech, and Signal Processing*, vol. 37, no. 7, pp. 984–995, July 1989.

[2] Z. Kassas, J. Khalife, K. Shamaei, and J. Morales, "I hear, therefore I know where I am: Compensating for GNSS limitations with cellular signals," *IEEE Signal Processing Magazine*, pp. 111–124, September 2017.

[3] A. Abdallah, K. Shamaei, and Z. Kassas, "Indoor positioning based on LTE carrier phase measurements and an inertial measurement unit," in *Proceedings of ION GNSS Conference*, September 2018, pp. 3374–3384.

[4] Federal Communications Commission, "Wireless E911 location accuracy requirements," https://apps.fcc.gov/edocspublic/attachmatch/FCC-15-9A1, February 2015.

[5] Y. Shu, Y. Huang, J. Zhang, P. Coue, P. Cheng, J. Chen, and K. Shin, "Gradient-based fingerprinting for indoor localization and tracking," *IEEE Transactions on Industrial Electronics*, vol. 63, no. 4, pp. 2424–2433, 2016.

[6] F. Wang, J. Feng, Y. Zhao, X. Zhang, S. Zhang, and J. Han, "Joint activity recognition and indoor localization with WiFi fingerprints," *IEEE Access*, vol. 7, pp. 80 058–80 068, 2019.

[7] Z. Zhang, S. He, Y. Shu, and Z. Shi, "A self-evolving WiFi-based indoor navigation system using smartphones," *IEEE Transactions on Mobile Computing*, vol. 19, no. 8, pp. 1760–1774, 2020.

[8] U. Schatzberg, L. Banin, and Y. Amizur, "Enhanced WiFi ToF indoor positioning system with MEMS-based INS and pedometric information," in *Proceedings of IEEE/ION Position, Location and Navigation Symposium*, May 2014, pp. 185–192.

[9] Y. Zhuang, Y. Li, L. Qi, H. Lan, J. Yang, and N. El-Sheimy, "A two-filter integration of MEMS sensors and WiFi fingerprinting for indoor positioning," *IEEE Sensors Journal*, vol. 16, no. 13, pp. 5125–5126, 2016.

[10] Y. Zhuang and N. El-Sheimy, "Tightly-coupled integration of WiFi and MEMS sensors on handheld devices for indoor pedestrian navigations," *IEEE Sensors Journal*, vol. 16, no. 1, pp. 224–234, 2016.

[11] J. Fiorina and W. Hachem, "On the asymptotic distribution of the correlation receiver output for time-hopped UWB signals," *IEEE Transactions on Signal Processing*, vol. 54, no. 7, pp. 2529–2545, 2006.

[12] C. Morelli, M. Nicoli, V. Rampa, and U. Spagnolini, "Hidden markov models for radio localization in mixed LOS/NLOS conditions," *IEEE Transactions on Signal Processing*, vol. 55, no. 4, pp. 1525–1542, 2007.

[13] C. Steiner and A. Wittneben, "Low complexity location fingerprinting with generalized UWB energy detection receivers," *IEEE Transactions on Signal Processing*, vol. 58, no. 3, pp. 1756–1767, 2010.

[14] O. Bialer, D. Raphaeli, and A. Weiss, "Efficient time of arrival estimation algorithm achieving maximum likelihood performance in dense multipath," *IEEE Transactions on Signal Processing*, vol. 60, no. 3, pp. 1241–1252, 2012.

[15] Y. Xu, Y. Shmaliy, Y. Li, and X. Chen, "UWB-based indoor human localization with time-delayed data using EFIR filtering," *IEEE Access*, vol. 5, pp. 16 676–16 683, 2017.

[16] C. Yao and W. Hsia, "An indoor positioning system based on the dual-channel passive RFID technology," *IEEE Transactions on Instrumentation and Measurement*, vol. 18, no. 11, pp. 4654–4663, 2018.

[17] Y. Zeng, X. Chen, R. Li, and H. Tan, "UHF RFID indoor positioning system with phase interference model based on double tag array," *IEEE Access*, vol. 7, pp. 76 768–76 778, 2019.

[18] C. Gentner, E. Munoz, M. Khider, E. Staudinger, S. Sand, and A. Dammann, "Particle filter based positioning with 3GPP-LTE in indoor environments," in *Proceedings of IEEE/ION Position, Location and Navigation Symposium*, April 2012, pp. 301–308.

[19] M. Driusso, C. Marshall, M. Sabathy, F. Knutti, H. Mathis, and F. Babich, "Indoor positioning using LTE signals," in *Proceedings of International Conference on Indoor Positioning and Indoor Navigation*, October 2016, pp. 1–8.

[20] A. Abdallah and Z. Kassas, "Evaluation of feedback and feedforward coupling of synthetic aperture navigation with LTE signals," in *Proceedings of IEEE Vehicular Technology Conference*, September 2019, pp. 1–6.

[21] A. Abdallah, K. Shamaei, and Z. Kassas, "Performance characterization of an indoor localization system with LTE code and carrier phase measurements and an IMU," in *Proceedings of International Conference on Indoor Positioning and Indoor Navigation*, September 2019, pp. 1–8.

[22] Z. Kassas, "Collaborative opportunistic navigation," *IEEE Aerospace and Electronic Systems Magazine*, vol. 28, no. 6, pp. 38–41, 2013.

[23] A. Coluccia and A. Fascista, "A review of advanced localization techniques for crowdsensing wireless sensor networks," *Sensors*, vol. 19, no. 5, pp. 988–1017, 2019.

[24] N. Souli, P. Kolios, and G. Ellinas, "Online relative positioning of autonomous vehicles using signals of opportunity," *IEEE Transactions on Intelligent Vehicles*, pp. 1–1, 2021.

[25] J. Raquet *et al.*, "Position, navigation, and timing technologies in the 21st century," J. Morton, F. van Diggelen, J. Spilker, Jr., and B. Parkinson, Eds. Wiley-IEEE, 2021, vol. 2, Part D: Position, Navigation, and Timing Using Radio Signals-of-Opportunity, ch. 35–43, pp. 1115–1412.

[26] Z. Kassas, "Position, navigation, and timing technologies in the 21st century," J. Morton, F. van Diggelen, J. Spilker, Jr., and B. Parkinson, Eds. Wiley-IEEE, 2021, vol. 2, ch. 38: Navigation with Cellular Signals of Opportunity, pp. 1171–1223.

[27] Z. Kassas, J. Khalife, A. Abdallah, and C. Lee, "I am not afraid of the jammer: navigating with signals of opportunity in GPS-denied environments," in *Proceedings of ION GNSS Conference*, 2020, pp. 1566–1585.

[28] A. Abdallah, J. Khalife, and Z. Kassas, "Experimental characterization of received 5G signals carrier-to-noise ratio in indoor and urban environments," in *Proceedings of IEEE Vehicular Technology Conference*, April 2021, pp. 1–5.

[29] C. Gentner, T. Jost, W. Wang, S. Zhang, A. Dammann, and U. Fiebig, "Multipath assisted positioning with simultaneous localization and mapping," *IEEE Transactions on Wireless Communications*, vol. 15, no. 9, pp. 6104–6117, September 2016.

[30] M. Driusso, C. Marshall, M. Sabathy, F. Knutti, H. Mathis, and F. Babich, "Vehicular position tracking using LTE signals," *IEEE Transactions on Vehicular Technology*, vol. 66, no. 4, pp. 3376–3391, April 2017.

[31] J. del Peral-Rosado, J. López-Salcedo, F. Zanier, and G. Seco-Granados, "Position accuracy of joint time-delay and channel estimators in LTE networks," *IEEE Access*, vol. 6, pp. 25 185–25 199, 2018.

[32] K. Shamaei, J. Morales, and Z. Kassas, "Positioning performance of LTE signals in Rician fading environments exploiting antenna motion," in *Proceedings of ION GNSS Conference*, September 2018, pp. 3423–3432.

[33] K. Shamaei, J. Khalife, and Z. Kassas, "A joint TOA and DOA approach for positioning with LTE signals," in *Proceedings of IEEE/ION Position, Location, and Navigation Symposium*, April 2018, pp. 81–91.

[34] S. Han, T. Kang, and J. Seo, "Smartphone application to estimate distances from LTE base stations based on received signal strength measurements," in *International Technical Conference on Circuits/Systems, Computers and Communications*, June 2019, pp. 1–3.

[35] P. Gadka, J. Sadowski, and J. Stefanski, "Detection of the first component of the received LTE signal in the OTDoA method," *Wireless Communications and Mobile Computing*, pp. 1–12, April 2019.

[36] T. Kang, H. Lee, and J. Seo, "TOA-based ranging method using CRS in LTE signals," *Journal of Advanced Navigation Technology*, vol. 23, no. 5, pp. 437–443, October 2019.

[37] T. Kang, H. Lee, and J. Seo, "Analysis of the maximum correlation peak value and RSRQ in LTE signals according to frequency bands and sampling frequencies," in *International Conference on Control, Automation and Systems*, October 2019, pp. 1182–1186.

[38] H. Lee, A. Abdallah, J. Park, J. Seo, , and Z. Kassas, "Neural network-based ranging with LTE channel impulse response for localization in indoor environments," in *Proceedings of International Conference on Control, Automation, and Systems*, October 2020, pp. 939–944.

[39] P. Wang and Y. Morton, "Multipath estimating delay lock loop for LTE signal TOA estimation in indoor and urban environments," *IEEE Transactions on Wireless Communications*, vol. 19, no. 8, pp. 5518–5530, 2020.

[40] P. Wang and Y. Morton, "Performance comparison of time-of-arrival estimation techniques for LTE signals in realistic multipath propagation channels," *NAVIGATION, Journal of the Institute of Navigation*, vol. 67, no. 4, pp. 691–712, December 2020.

[41] H. Dun, C. Tiberius, and G. Janssen, "Positioning in a multipath channel using OFDM signals with carrier phase tracking," *IEEE Access*, vol. 8, pp. 13 011–13 028, 2020.

[42] K. Avval, "Cellular-based localization for mobile devices with structured motion," Master's thesis, University of Toronto, Canada, 2020.

[43] A. Graff, W. Blount, P. Iannucci, J. Andrews, and T. Humphreys, "Analysis of OFDM signals for ranging and communications," in *Proceedings of ION GNSS Conference*, September 2021, pp. 2910–2924.

[44] T. Kazaz, G. Janssen, J. Romme, and A. Van der Veen, "Delay estimation for ranging and localization using multiband channel state information," *IEEE Transactions on Wireless Communications*, pp. 1–16, September 2021.

[45] K. Shamaei and Z. Kassas, "Receiver design and time of arrival estimation for opportunistic localization with 5G signals," *IEEE Transactions on Wireless Communications*, vol. 20, no. 7, pp. 4716–4731, 2021.

[46] J. del Peral-Rosado, R. Estatuet-Castillo, J. Lopez-Salcedo, G. Seco-Granados, Z. Chaloupka, L. Ries, and J. Garcoa-Molina, "Evaluation of hybrid positioning scenarios for autonomous vehicle applications," in *Proceedings of ION International Technical Meeting Conference*, January 2017, pp. 2541–2553.

[47] F. Pittino, M. Driusso, A. Torre, and C. Marshall, "Outdoor and indoor experiments with localization using LTE signals," in *Proceedings of European Navigation Conference*, May 2017, pp. 311–321.

[48] Z. Kassas, J. Morales, K. Shamaei, and J. Khalife, "LTE steers UAV," *GPS World Magazine*, vol. 28, no. 4, pp. 18–25, April 2017.

[49] K. Shamaei, J. Khalife, and Z. Kassas, "Exploiting LTE signals for navigation: Theory to implementation," *IEEE Transactions on Wireless Communications*, vol. 17, no. 4, pp. 2173–2189, April 2018.

[50] K. Shamaei and Z. Kassas, "LTE receiver design and multipath analysis for navigation in urban environments," *NAVIGATION, Journal of the Institute of Navigation*, vol. 65, no. 4, pp. 655–675, December 2018.

[51] K. Shamaei, J. Khalife, and Z. Kassas, "Pseudorange and multipath analysis of positioning with LTE secondary synchronization signals," in *Proceedings of Wireless Communications and Networking Conference*, April 2018, pp. 286–291.

[52] K. Shamaei, J. Morales, and Z. Kassas, "A framework for navigation with LTE time-correlated pseudorange errors in multipath environments," in *Proceedings of IEEE Vehicular Technology Conference*, April 2019, pp. 1–6.

[53] J. Mortier, G. Pages, and J. Vila-Valls, "Robust TOA-based UAS navigation under model mismatch in GNSS-denied harsh environments," *Remote Sensing*, vol. 12, no. 18, pp. 2928–2947, September 2020.

[54] M. Maaref and Z. Kassas, "Measurement characterization and autonomous outlier detection and exclusion for ground vehicle navigation with cellular signals," *IEEE Transactions on Intelligent Vehicles*, vol. 5, no. 4, pp. 670–683, December 2020.

[55] Z. Kassas, M. Maaref, J. Morales, J. Khalife, and K. Shamaei, "Robust vehicular localization and map matching in urban environments through IMU, GNSS, and cellular signals," *IEEE Intelligent Transportation Systems Magazine*, vol. 12, no. 3, pp. 36–52, June 2020.

[56] J. Khalife and Z. Kassas, "Opportunistic UAV navigation with carrier phase measurements from asynchronous cellular signals," *IEEE Transactions on Aerospace and Electronic Systems*, vol. 56, no. 4, pp. 3285–3301, August 2020.

[57] S. Ragothaman, M. Maaref, and Z. Kassas, "Autonomous ground vehicle path planning in urban environments using GNSS and cellular signals reliability maps: Models and algorithms," *IEEE Transactions on Aerospace and Electronic Systems*, vol. 57, no. 2, pp. 1562–1580, 2021.

[58] S. Ragothaman, M. Maaref, and Z. Kassas, "Autonomous ground vehicle path planning in urban environments using GNSS and cellular signals reliability maps: Simulation and experimental results," *IEEE Transactions on Aerospace and Electronic Systems*, vol. 57, no. 4, pp. 2575–2586, 2021.

[59] J. Khalife and Z. Kassas, "Precise UAV navigation with cellular carrier phase measurements," in *Proceedings of IEEE/ION Position, Location, and Navigation Symposium*, April 2018, pp. 978–989.

[60] K. Shamaei and Z. Kassas, "Sub-meter accurate UAV navigation and cycle slip detection with LTE carrier phase," in *Proceedings of ION GNSS Conference*, September 2019, pp. 2469–2479.

[61] J. Khalife and Z. Kassas, "On the achievability of submeter-accurate UAV navigation with cellular signals exploiting loose network synchronization," *IEEE Transactions on Aerospace and Electronic Systems*, 2022, accepted.

[62] Z. Kassas, J. Khalife, A. Abdallah, and C. Lee, "I am not afraid of the GPS jammer: resilient navigation via signals of opportunity in GPS-denied environments," *IEEE Aerospace and Electronic Systems Magazine*, 2022, accepted.

[63] C. Gentner, "Channel-SLAM: Multipath assisted positioning," Ph.D. dissertation, Ulm University, 2018.

[64] S. Bose and A. Steinhardt, "Adaptive array detection of uncertain rank one waveforms," *IEEE Transactions on Signal Processing*, vol. 44, no. 11, pp. 2801–2809, 1996.

[65] Y. Zhang, B. Obeidat, and M. Amin, "Spatial polarimetric time-frequency distributions for direction-of-arrival estimations," *IEEE Transactions on Signal Processing*, vol. 54, no. 4, pp. 1327–1340, 2006.

[66] Z. Zhang and C. Law, "Short-delay multipath mitigation technique based on virtual multipath," *IEEE Antennas and Wireless Propagation Letters*, vol. 4, pp. 344–348, 2005.

[67] M. Sanchez-Fernandez, M. Aguilera-Forero, and A. Garcia-Armada, "Performance analysis and parameter optimization of DLL and MEDLL in fading multipath environments for next generation navigation receivers," *IEEE Transactions on Consumer Electronics*, vol. 53, no. 4, pp. 1302–1308, November 2007.

[68] C. Chen, G. Chang, N. Zheng, and T. Xu, "GNSS multipath error modeling and mitigation by using sparsity-promoting regularization," *IEEE Access*, vol. 7, pp. 24 096–24 108, November 2019.

[69] Y. Wang, Y. Wu, and Y. Shen, "Joint spatiotemporal multipath mitigation in large-scale array localization," *IEEE Transactions on Signal Processing*, vol. 67, no. 3, pp. 783–797, February 2019.

[70] Z. Chen, G. Gokeda, and Y. Yu, *Introduction to Direction-of-arrival Estimation*. Artech House, 2010.

[71] S. Draganov, M. Harlacher, L. Haas, M. Wenske, and C. Schneider, "Synthetic aperture navigation in multipath environments," *IEEE Wireless Communications*, vol. 18, no. 2, pp. 52–58, April 2011.

[72] S. Daneshmand, A. Broumandan, N. Sokhandan, and G. Lachapelle, "GNSS multipath mitigation with a moving antenna array," *IEEE Transactions on Aerospace and Electronic Systems*, vol. 49, no. 1, pp. 693–698, January 2013.

[73] A. Abdallah, K. Shamaei, and Z. Kassas, "Indoor localization with LTE carrier phase measurements and synthetic aperture antenna array," in *Proceedings of ION GNSS Conference*, September 2019, pp. 2670–2679.

[74] L. Haas and M. Harlacher, "First responder location and tracking using synthetic aperture navigation," in *Proceedings of IEEE/ION Position, Location and Navigation Symposium*, 2010, pp. 483–487.

[75] W. Leong, K. Patel, J. Weinfield, and D. Karnick, "Synthetic aperture navigation algorithms applied to a driving user in multipath environments," in *Proceedings of IEEE/ION Position, Location and Navigation Symposium*, 2012, pp. 673–677.

[76] A. Broumandan, J. Nielsen, and G. Lachapelle, "Enhanced detection performance of indoor GNSS signals based on synthetic aperture," *IEEE Transactions on Vehicular Technology*, vol. 59, no. 6, pp. 2711–2724, July 2010.

[77] K. Pahlavan, P. Krishnamurthy, and A. Beneat, "Wideband radio propagation modeling for indoor geolocation applications," *IEEE Communications Magazine*, vol. 36, no. 4, pp. 60–65, 1998.

[78] W. Xu, Z. Wang, and S. Zekavat, *Handbook of Position Location: Theory, Practice, and Advances*, September 2011, ch. An Introduction to NLOS Identification and Localization, pp. 523–555.

[79] X. Cai, X. Li, R. Yuan, and Y. Hei, "Identification and mitigation of NLOS based on channel state information for indoor WiFi localization," in *Proceedings of International Conference on Wireless Communications Signal Processing*, October 2015, pp. 1–5.

[80] P. Misra and P. Enge, *Global Positioning System: Signals, Measurements, and Performance*, 2nd ed. Ganga-Jamuna Press, 2010.

[81] F. Duan, B. Chapeau-Blondeau, and D. Abbott, "Weak signal detection: condition for noise induced enhancement," *Digital Signal Processing*, vol. 23, no. 5, pp. 1585–1591, 2013.

[82] P. Groves and Z. Jiang, "Height aiding, $c/n0$ weighting and consistency checking for GNSS NLOS and multipath mitigation in urban areas," *NAVIGATION, Journal of the Institute of Navigation*, vol. 66, no. 5, pp. 653–669, 2013.

[83] N. Dwek, M. Birem, K. Geebelen, E. Hostens, A. Mishra, J. Steckel, and R. Yudanto, "Improving the accuracy and robustness of ultra-wideband localization through sensor fusion and outlier detection," *IEEE Robotics and Automation Letters*, vol. 5, no. 1, pp. 32–39, 2019.

[84] 3GPP, "Evolved universal terrestrial radio access (E-UTRA); physical channels and modulation," 3rd Generation Partnership Project (3GPP), TS 36.211, January 2011. [Online]. Available: http://www.3gpp.org/ftp/Specs/html-info/36211.htm

[85] 3GPP, "Evolved universal terrestrial radio access (E-UTRA); requirements for support of radio resource management," 3rd Generation Partnership Project (3GPP), TS 36.133, April 2010. [Online]. Available: www.3gpp.org/dynareport/36133.htm

[86] M. Speth, S. Fechtel, G. Fock, and H. Meyr, "Optimum receiver design for wireless broad-band systems using OFDM. I," *IEEE Transactions on Communications*, vol. 47, no. 11, pp. 1668–1677, November 1999.

[87] B. Yang, K. Letaief, R. Cheng, and Z. Cao, "Timing recovery for OFDM transmission," *IEEE Journal on Selected Areas in Communications*, vol. 18, no. 11, pp. 2278–2291, November 2000.

[88] E. Kaplan and C. Hegarty, *Understanding* GPS*: Principles and Applications*, 2nd ed. Artech House, 2005.

[89] "Septentrio AsteRx-i V," https://www.septentrio.com/products, 2018.

[90] J. Morales and Z. Kassas, "Optimal collaborative mapping of terrestrial transmitters: receiver placement and performance characterization," *IEEE Transactions on Aerospace and Electronic Systems*, vol. 54, no. 2, pp. 992–1007, April 2018.

[91] J. Morales, J. Khalife, and Z. Kassas, "GNSS vertical dilution of precision reduction using terrestrial signals of opportunity," in *Proceedings of ION International Technical Meeting Conference*, January 2016, pp. 664–669.

[92] J. Morales, J. Khalife, and Z. Kassas, "Opportunity for accuracy," *GPS World Magazine*, vol. 27, no. 3, pp. 22–29, March 2016.

[93] Z. Kassas, V. Ghadiok, and T. Humphreys, "Adaptive estimation of signals of opportunity," in *Proceedings of ION GNSS Conference*, September 2014, pp. 1679–1689.

[94] W. Lee, *Mobile cellular telecommunications: analog and digital systems*. New York, USA: McGraw-Hill Professional, 1995.

[95] A. Saleh and R. Valenzuela, "A statistical model for indoor multipath propagation," *IEEE Journal on Selected Areas in Communications*, vol. 5, no. 2, pp. 128–137, February 1987.

[96] J. Litva and T. Lo, *Digital beamforming in wireless communications*. Boston, London: Artech House, 1996.

[97] S. Hyeon, Y. Yun, H. Kim, and S. Choi, "Phase diversity for an antenna-array system with a short interelement separation," *IEEE Transactions on Vehicular Technology*, vol. 57, no. 1, pp. 206–214, 2008.

[98] A. Broumandan, "Enhanced narrowband signal detection and estimation with a synthetic antenna array for location applications," Ph.D. dissertation, University of Calgary, Canada, 2009.

[99] A. Abdallah and Z. Kassas, "Deep learning-aided spatial discrimination for multipath mitigation," in *Proceedings of IEEE/ION Position, Location, and Navigation Symposium*, April 2020, pp. 1324–1335.

[100] R. Schmidt, "Multiple emitter location and signal parameter estimation," *IEEE Transactions on Antennas and Propagation*, vol. 34, no. 3, pp. 276–280, March 1986.

[101] S. Pillai and B. Kwon, "Forward/backward spatial smoothing techniques for coherent signal identification," *IEEE Transactions on Acoustics, Speech, and Signal Processing*, vol. 37, no. 1, pp. 8–15, January 1989.

[102] M. Wax and I. Ziskind, "Detection of the number of coherent signals by the MDL principle," *IEEE Transactions on Acoustics, Speech, and Signal Processing*, vol. 37, no. 8, pp. 1190–1196, August 1989.

[103] W. Pan, "Akaike's information criterion in generalized estimating equations," *Biometrics*, vol. 57, no. 1, pp. 120–125, March 2001.

[104] J. Rissanen, "Modeling by shortest data description," *Automatica*, vol. 14, no. 5, pp. 465–471, September 2019.

[105] M. Zoltowski, "On the performance analysis of the MVDR beamformer in the presence of correlated interference," *IEEE Transactions on Acoustics, Speech, and Signal Processing*, vol. 36, no. 6, pp. 945–947, 1988.

[106] C. Pan, J. Chen, and J. Benesty, "Performance study of the MVDR beamformer as a function of the source incidence angle," *IEEE/ACM Transactions on Audio, Speech, and Language Processing*, vol. 22, no. 1, pp. 67–79, 2014.

[107] A. Abdallah and Z. Kassas, "Multipath mitigation via synthetic aperture beamforming for indoor and deep urban navigation," *IEEE Transactions on Vehicular Technology*, vol. 70, no. 9, pp. 8838–8853, September 2021.

[108] A. Abdallah, C. Jao, Z. Kassas, and A. Shkel, "A pedestrian indoor navigation system using deep-learning-aided cellular signals and ZUPT-aided foot-mounted IMUs," *IEEE Sensors Journal*, vol. 22, no. 6, pp. 5188–5198, march 2022.

[109] J. Morales, P. Roysdon, and Z. Kassas, "Signals of opportunity aided inertial navigation," in *Proceedings of ION GNSS Conference*, September 2016, pp. 1492–1501.

[110] J. Morales and Z. Kassas, "Tightly-coupled inertial navigation system with signals of opportunity aiding," *IEEE Transactions on Aerospace and Electronic Systems*, vol. 57, no. 3, pp. 1930–1948, 2021.

[111] J. Khalife, K. Shamaei, S. Bhattacharya, and Z. Kassas, "Centimeter-accurate UAV navigation with cellular signals," in *Proceedings of ION GNSS Conference*, September 2018, pp. 2321–2331.

[112] K. Pesyna, Z. Kassas, J. Bhatti, and T. Humphreys, "Tightly-coupled opportunistic navigation for deep urban and indoor positioning," in *Proceedings of ION GNSS Conference*, September 2011, pp. 3605–3617.

[113] Z. Kassas and T. Humphreys, "Observability analysis of collaborative opportunistic navigation with pseudorange measurements," *IEEE Transactions on Intelligent Transportation Systems*, vol. 15, no. 1, pp. 260–273, February 2014.

[114] Z. Kassas, "Analysis and synthesis of collaborative opportunistic navigation systems," Ph.D. dissertation, The University of Texas at Austin, USA, 2014.

[115] Z. Kassas and T. Humphreys, "Receding horizon trajectory optimization in opportunistic navigation environments," *IEEE Transactions on Aerospace and Electronic Systems*, vol. 51, no. 2, pp. 866–877, April 2015.

[116] Z. Kassas, A. Arapostathis, and T. Humphreys, "Greedy motion planning for simultaneous signal landscape mapping and receiver localization," *IEEE Journal of Selected Topics in Signal Processing*, vol. 9, no. 2, pp. 247–258, March 2015.

[117] C. Yang and A. Soloviev, "Simultaneous localization and mapping of emitting radio sources-SLAMERS," in *Proceedings of ION GNSS Conference*, September 2015, pp. 2343–2354.

[118] J. Morales and Z. Kassas, "Stochastic observability and uncertainty characterization in simultaneous receiver and transmitter localization," *IEEE Transactions on Aerospace and Electronic Systems*, vol. 55, no. 2, pp. 1021–1031, April 2019.

[119] C. Yang and A. Soloviev, "Mobile positioning with signals of opportunity in urban and urban canyon environments," in *Proceedings of IEEE/ION Position, Location, and Navigation Symposium*, April 2020, pp. 1043–1059.

[120] K. Shamaei, J. Khalife, S. Bhattacharya, and Z. Kassas, "Computationally efficient receiver design for mitigating multipath for positioning with LTE signals," in *Proceedings of ION GNSS Conference*, September 2017, pp. 3751–3760.

[121] F. Daum, "Nonlinear filters: Beyond the Kalman filter," *IEEE Aerospace and Electronic Systems Magazine*, vol. 20, no. 8, pp. 57–69, 2005.

[122] C. Montella, "The Kalman filter and related algorithms: A literature review," *Research Gate*, 2011.